university of groningen

faculty of science and engineering

# On the Path to Cosmic Web Genesis

*Author:*
Maria-Ruxandra NĂSTASE
*(s4900294)*

*Supervisor:*
prof. dr. M.A.M. (Rien) VAN DE WEIJGAERT
*Second examiner :*
prof. dr. Emanuela DIMASTROGIOVANNI

Bachelor's Thesis
To fulfill the requirements for the degree of
Bachelor of Science in Physics
at the University of Groningen

July 2, 2024

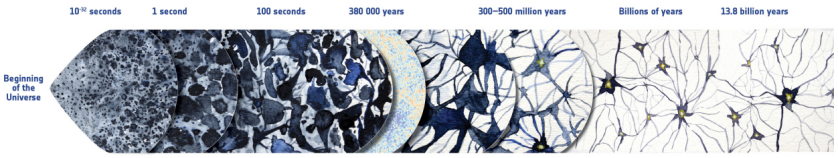

# Contents

# Abstract

The goal of this research was to analyse mass transport in Cosmic Web environments from early, proto-structure redshifts to present time. Following the rationale of anisotropic gravitational collapse, the Zel'dovich approximation defines a clear sequence of mass migration based on deformation tensor eigenvalues. Particles move from underdense regions into denser ones, i.e. from voids to their surrounding walls, to the filaments that interconnect them and finally end up in highly dense clusters.

To investigate this phenomenon, data from the Illustris 3 Dark simulation was processed with the Delaunay Tesselation Field Estimator (DTFE) and with the NEXUS+ programs developed by Marius Cautun. With DTFE the discrete data-point data from Illustris was converted to a continuously defined density field which allowed a higher resolution analysis and maintained geometrical and hierarchical information about the density distribution, crucial for NEXUS+ characterisation. Subsequently, using the density field as input, NEXUS+ was able to identify the various morphological components (walls, filaments, clusters and voids) **in a scale-independent manner** at each point in the field. Finally, a script was created that allowed the association of an Illustris particle ID with its NEXUS+ identified environment tag. This made it possible to follow the evolution as well as to observe the history of mass flow for each environment. Two directions were therefore of interest: the particles presently associated with a particular environment (i.e. at $z = 0$) were followed back in time (to a redshift of $z = 5$); and the reverse was done- identifying the environment type a mass particle could be found in at an earlier time and analysing its sequential progression with time.

A good general agreement was found between the sequence of mass collapse predicted by the Zel'dovich approximation and environment transport identified by NEXUS+. A more complete way to study mass transport across different morphological components could be carried out in future research. This could entail large-scale velocity field analysis, since it dictates mass element flows and could shed light onto the discrepancies found.

# Acknowledgments

I have many people to thank for helping me along the way, but first and foremost of course prof. van Weygaert, without whose support this project would not have been possible. He pushed us to be creative in exploring our problem and to think deeper about its implications. I would also like to thank prof. Dimastrogiovanni for her time and support.

I thank my colleague Călin M. Ghizdaveț for sharing a script that converted the illustris file format .hdf5 to .gadget format and my colleague Ivan Spirov for his brilliant idea that helped me use illustris data to match particle IDs to their respective environment, when the alternative method stopped being a viable option.

This acknowledgement section would not be complete without me thanking my beloved, Călin Anca, whose consultancy services got me across the finish line on time.

More gratitude is in order for the people involved at brain.fm and to those involved in the creation of noise-cancelling technologies whom have all contributed their due to my writing of this piece.

The picture on the cover is from ESA.

The following is part of a poem that is, at first glance, about unfulfilled, romantic love, but like all good poetry, it leaves the beholder freedom of interpretation. As such, I will give the reader the same courtesy, not burdening them with my own, in hopes that they simply enjoy it.

*Luceafărul by M. Eminescu*

Și-i zise-ncet: - ”Încă de mic
Te cunoșteam pe tine,
Și guraliv și de nimic,
Te-ai potrivi cu mine...
Dar un luceafar, răsărit
Din liniștea uitării,
Dă orizon nemărginit
Singurătații mării.
Și tainic genele le plec,
Căci mi le împle plînsul
Când ale apei valuri trec
Călătorind spre dînsul.

Lucește c-un amor nespus,
Durerea să-mi alunge,
Dar se înalță tot mai sus,
Ca să nu-l pot ajunge.
Pătrunde trist cu raze reci
Din lumea ce-l desparte...
În veci îl voi iubi și-n veci
Va rămînea departe...
De-aceea zilele îmi sunt
Pustii ca niște stepe,
Dar nopțile-s de-un farmec sfânt
Ce-l nu mai pot pricepe. ”

# 1 Introduction

The majestic and intricate tapestry of the cosmic web weaves together the vast expanse of the Universe. Stretching across spacetime, the cosmic web is a breathtaking network of immense voids, luminous filaments, grand walls, and highly dense nodes. It is the Universe's grandest structure, marking the transition from the primordial matter distribution, from which everything emerged, to the scale at which non-linear structures start at form and galaxies and stars are born. This colossal and intricate pattern not only showcases the beauty of the cosmos but also holds the secrets to the origins and evolution of the Universe itself. This thesis aims to explore this grandiose structure and its evolution by following it in time- from its infancy in the cosmic microwave background radiation with its minor density perturbations, through to its period of anisotropic gravitational collapse, finally tracing the mass transports responsible for the emerging Cosmic Web.

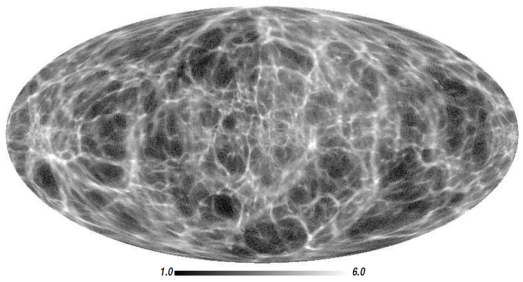


Figure 1: Detailed reconstruction of the local dark matter Cosmic Web, courtesy of [1]

On scales of around $100$ [Mpc] [2], the Cosmic Web displays its spider web resembling structure, composed of **voids**, **filaments**, **walls** and **nodes**. [3, 4] Voids are immense under-dense regions, encased by walls and filaments, which interconnect nodes where massive galaxy clusters reside.[5] Being high-density regions, these latter objects contain most of the mass found in the web, but most of the volume is occupied by voids [6, 7], as can be seen in figure 1 (reconstructed dark matter), figure 2 (observational data) and later on in figure 9 (simulation data). It is important to note, however, that on scales larger than this, the Universe has other interesting properties: it is **homogeneous** and **isotropic**. Together, these traits make up the ***Cosmological Principle*** [2], a powerful assumption that reveals fundamental properties of the space we inhabit, for instance that only 3 types of physical space are possible with these conditions in mind: flat, hyperbolic or spherical. This has led to important constraints on the theories we can create to untangle the Universe's mysteries. In essence, we want to look at how the Universe turns from an almost perfectly isotropic and homogeneous field to what it is today: an intricate web of substantially dense nodes and vast empty void regions connected by walls and filaments.

For billions of years, the Universe has been changing, being molded into the complex patterns observed in the cosmic web. As we will see, it is the result of anisotropic gravitational collapse, the process through which structure forms [9], acting on the imperfectly uniform density field of the primordial Universe. N-body computer simulations have revealed the large-scale structure of the cosmos evolving into a complex and detailed web of filaments, punctuated by dense, compact clusters at the intersections of the network. [10, 11, 12, 13, 14, 15, 16] The structures form in a hierarchical

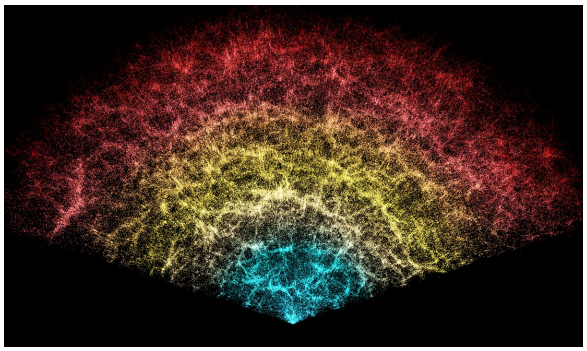

Figure 2: Slice of 3D galaxy map collected by the DESI survey, courtesy of [8]

manner [17, 18, 12], at considerably different scales of density and length, making it difficult to identify and describe quantitatively. Still, it is a worthwhile endeavor, as these once tiny deviations from uniformity are believed to be the birthplace of galaxies, one of them being our own.

There have been many attempts at characterising this network of objects, starting with models that would give global and statistical information on the web, but that would give no information on localised or individual structure identification. More recent advances have ushered in different types of algorithms for detecting individual structures[1]. In this thesis I aim to use the NEXUS+ multi-scale morphology filter[7, 5] to identify environments in the Illustris Dark Matter 3 simulation (ILD3) at different redshift values. Doing so will give me the ability to reconstruct a history of mass transport between the different today's environments and the evolution of environments from redshift $z = 5.00$. In figure 3 we can see how mass migrates from lower density regions to higher density regions in the local Universe. We know that mass migration is the basis of large scale structure formation, making this an essential aspect to research for a better theoretical understanding of the phenomenon.

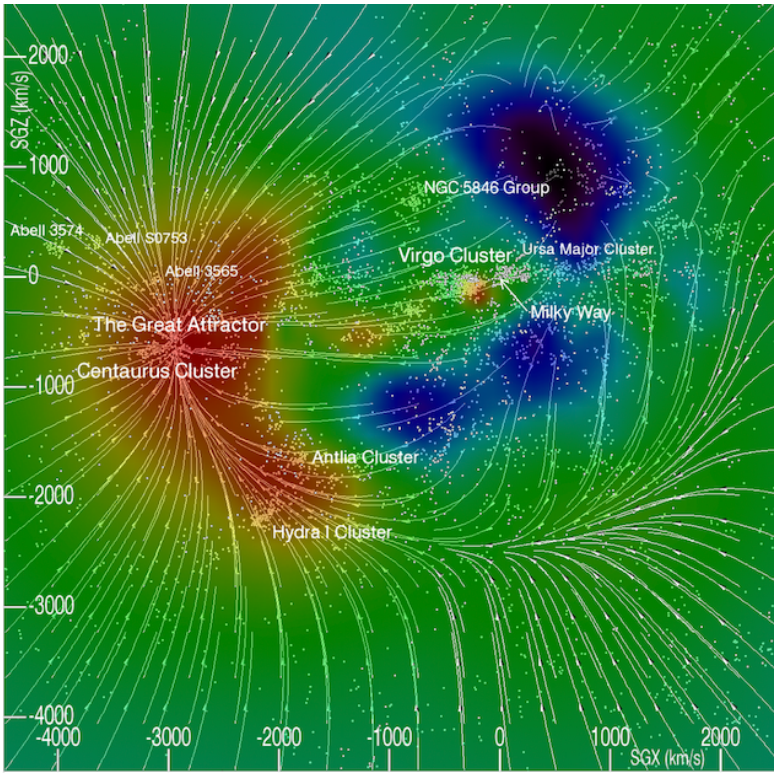


Figure 3: Cosmic flows and underlying velocity field, courtesy of [19]

## 1.1 Thesis Outline

Firstly, in section 2 we will go over the mechanisms responsible for the collapse of mass into intricate non-linear structures. In section 3 simulation information is given and some preliminary results are qualitatively assessed. Section 4 goes into some detail about the two programs used to process the illustris data and to identify the web environments, DTFE and NEXUS+ MMF respectively. Finally in section 5 we look at how mass elements are transported from one environment type to another.

[1] for a more detailed history consult [5]

# 2 Dynamics of Structure Formation

Observing the initial conditions of the Universe sets constraints on the parameters and theories we use to model it. The cosmic microwave background (CMB) radiation lets us gaze at the earliest observable "image" of the Universe in its infancy, roughly 380,000 years after the Big Bang [20]. The radiation in the CMB is within one part in $10^4$ to that of a blackbody and is nearly isotropic, varying with only 30mK across the sky. [2] A nearly isotropic blackbody background radiation presents a strong case for the Hot Big Bang model- the notion that the Universe was in a hot, dense and mostly uniform state at an earlier time. According to Bardeen et al., modelling the fluctuations in such a primordial density field to be distributed as random Gaussian, one obtains a strong analytical framework with which to address to issue of formation of large-scale structure from small initial density fluctuations.[21] To be precise, one expects nonlinear structure to form in the local maxima of the Gaussian random fields, agreeing with experiment. [21] Therefore, the large-scale cosmic structure that can be observed today is believed to have originated in the slight density fluctuations of the otherwise relatively homogeneous medium left behind after the inflation period. [3]

According to Peebles' cornerstone work on the matter, anisotropic gravitational collapse is the motor of matter formation. [9] To better understand this mechanism let us examine it through the lens of the Zel'dovich formalism of gravitational instability, an approximation for the "*growth of perturbations during the expansion of matter without pressure*" [22], which gives a good description of structure formation in the initial linear and up to mildly non-linear stages of structure formation, i.e. when $\delta\rho/\rho < 1$ [22]. According to this formalism, a clear sequence of collapse can be defined for regions based on the eigenvalues of their deformation tensor. The Zel'dovich approximation is a first-order Lagrangian approximation for the formation of matter in the Universe, predicting collapses by analysing mass element orbits under a Lagrangian approximation. It assumes, however, that the initial gravitational potential of the distribution does not change. The following derivation is from Cautun et al. [5]: at some time t, the Eulerian position of a mass element is given by:

| $\lambda_1$ | $\lambda_2$ | $\lambda_3$ | Component |
|---|---|---|---|
| + | + | + | Cluster |
| + | + | − | Filament |
| + | − | − | Sheet |
| − | − | − | Void |

Figure 4: Morphological segmentation of matter according to the Zel'dovich formalism with $\lambda_1 \geq \lambda_2 \geq \lambda_3$ as the eigenvalues of the deformation tensor; figure and description courtesy of [5]

$$\vec{x}(t) = \vec{q} + D(t)\nabla\varphi(\vec{q}) \tag{1}$$

where $\vec{q}$ is the Lagrangian position of the element, $D(t)$ is the linear growth factor and $\varphi(\vec{q})$ in the Lagrangian displacement potential (from [9]). With this in mind, we are able to map an initial mass element $\overline{\rho} d^3\vec{q}$ to a later time $\rho(\vec{x})d^3\vec{x}$ whilst conserving the mapped volume, equivalent to equating these two expressions. This yields:

$$\rho(\vec{x}) = \frac{\overline{\rho}}{[1 - D\,\lambda_1(\vec{q})][1 - D\,\lambda_2(\vec{q})][1 - D\,\lambda_3(\vec{q})]} \tag{2}$$

where we have the density at Eulerian position, $\rho(\vec{x})$ and $\overline{\rho}$ represents the mean cosmic density. The

three λ values represent the eigenvalues of the deformation tensor:

$$\varphi_{ij}(\vec{q}) = \frac{\partial^2 \varphi(\vec{q})}{\partial q_i \, q_j} \tag{3}$$

Cautun et al. beautifully summarises and visualizes these results. In figure 4 we can observe the dependence of the morphology of regions on the eigenvalues of the deformation tensor: regions with no positive values can be catalogued as voids, those with one, two and three positive value(s) correspond to sheets/walls, filaments and clusters/nodes respectively. In figure 5 the sequence of collapse can be seen. If we were to take some point masses to be perfectly uniformly spread in a sphere, we could easily imagine that the spherically symmetrical potential yields a situation of uniform collapse. There can, however, be no perfectly spherical regions in the Universe, as shown by [21], and the second-best approximation to that is an ellipsoid. If we now imagine an ellipsoidal region embedded with mass elements, it is natural that the major axis and minor axis would not feel the same force due to the now slightly asymmetric mass distribution- one axis will experience larger gravitational pull and will start contracting faster. Even the smallest divergence from a sphere would then cause a runaway process that prompts the region to collapse most strongly along one axis to form a sheet, succeeded by the contraction of the second axis to form a filament.[5] Finally the region completely collapses. What starts off as a slight initial local overdensity will follow this pattern of anisotropic collapse. By the same arguments, the reverse can be stated of a region that starts off as an underdenesity.

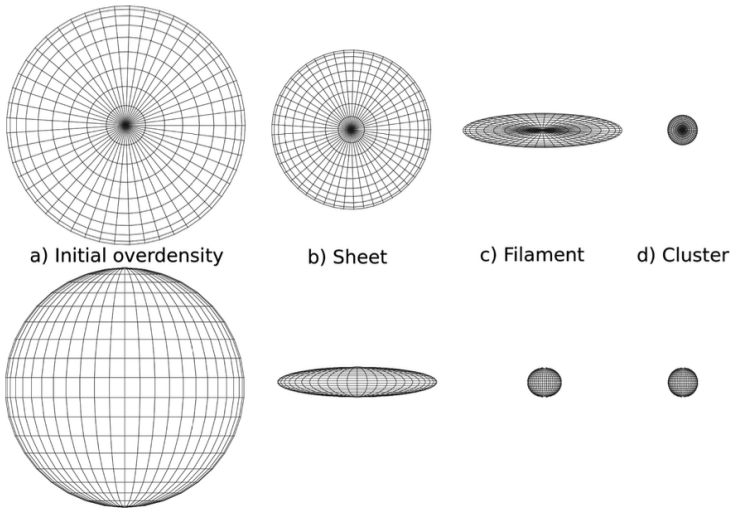


Figure 5: Structure formation according to Zel'dovich formalism; an initially overdense region of ellipsoidal shape as seen from two perpendicular axes will go through the sequence: sheet → filament → cluster (courtesy of [5])

On top of the gravitational instability experienced inside these regions which leads to their collapse, one can naturally assume that an overdense region embedded in an otherwise uniform field will attract more and more matter into it, becoming a larger and larger overdensity, to the point that it can no longer be approximated correctly in a linear fashion (i.e. $\delta\rho/\rho \not< 1$). By the nature of these processes, taking the initial perturbations in matter distribution seen from the CMB, we can start to qualitatively imagine how an intricate structure begins to form as matter makes its way from one morphological structure to another as time flows.

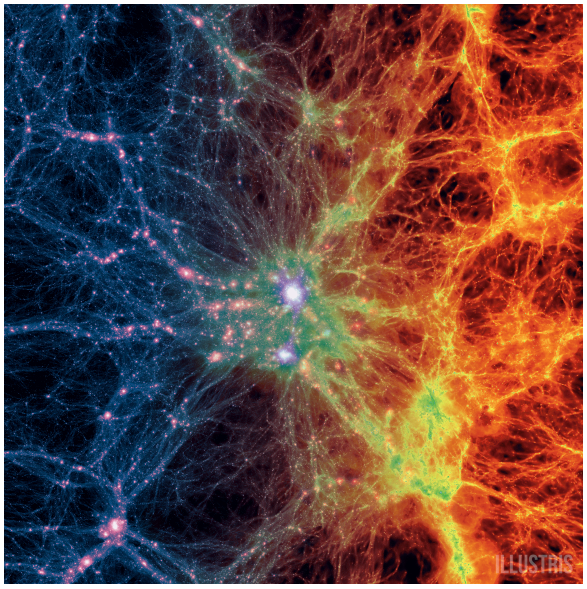


Figure 6: Image of the Cosmic Web obtained in the Illustris simulation [23] [24]

As the discussed framework is an approximation for the linear stage of cosmic structure formation, we are faced with the question of what happens when we leave the linear regime, where regions start to merge or collapse into each other and intricate patterns arise. A natural answer to this issue was ushered in by advances in computing power, which allow vast N-body computer experiments (simulations) to model what happens when analytical solutions reach their limits. It has been shown in N-body computer experiments (for instance by [10, 11, 12, 13, 14, 15, 16]), that the characteristic web-like pattern is a natural outcome of gravitational structure formation process. [25] It represents the departure from the primordial Gaussian field to the highly nonlinear structures we observe today. The emerging structure- the Cosmic Web- is central to our understanding of cosmic evolution. As can be seen in figure 6, from the Illustris simulation, the web consists of vast interconnected filaments, walls and voids. Its general properties include an **anisotropic configuration**, with elongated filamentary features as the dominant structural feature and flattened sheets or walls. Its **multiscale nature** can be seen in the range of scales and wide range of densities over which these structures form. The web also displays a clear **overdense-underdense asymmetry**, where voids are vast, roundish, unpopulated domains, taking up most of the volume, while filaments and walls are overdense and elongated or flattened and nodes (or clusters) are highly overdense and compact, making up for most of the mass.

The Cosmic Web has been mapped using observational surveys, such as the Sloan Digital Sky Survey (SDSS), and data from Cosmicflows- (I:IV), which provide maps of peculiar velocities and mass distributions of the local Universe. The flow of matter can be observed in figs. 7 and 8. In figure 7 the galaxies in the V8k catalogue [2] are plotted as black dots, and the vectors representing their velocities as gray lines. In figure 8, plot (a), we see flow-lines superimposed on the over-density field, coloured as a gradient from blue (under-dense) to red (over-dense). The colour of the stream-lines in both plots (a) and (b) represents the local speed. In panel (b) the V8k galaxies ([26]) are plotted as black dots [27]. These maps clearly reinforce the migration of mass in the local Universe. We can bypass some of the limitations associated with observational data by using simulations. These allow the visualisation of the evolution of proto-structures in the early Universe to the present day, giving us an idea of a much earlier history of the web than available by observation alone. The data obtained from simulations and observation collectively underscore the importance of the Cosmic Web and its evolution in understanding the formation of large-scale structure in the Universe.

[2] available at Extragalactic Distance Database (EDD)

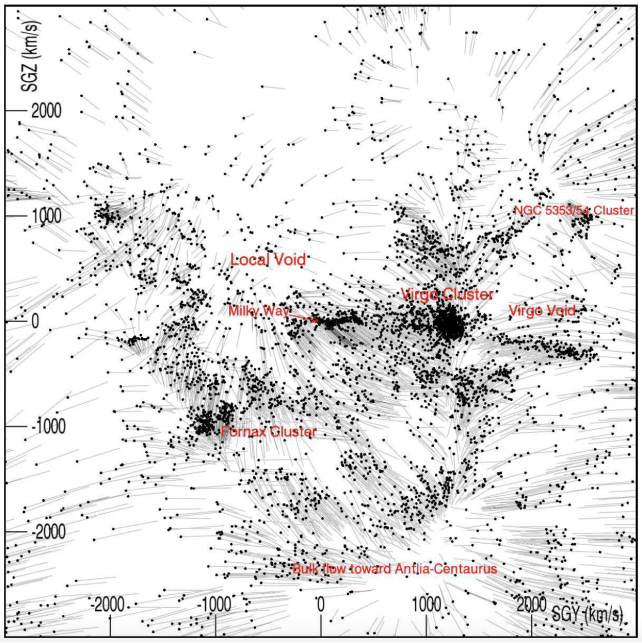


Figure 7: V8k galaxies shown as black dots, with vectors indicating their motion, courtesy of [19]

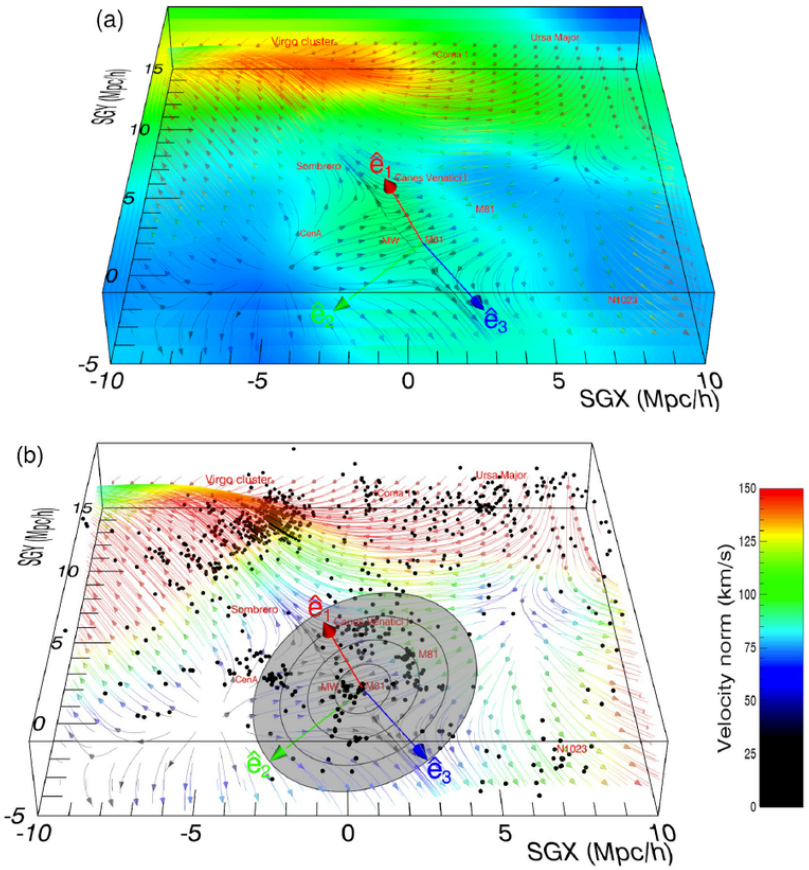


Figure 8: Peculiar velocity and over-density field; in (a) the overdesnity field with stream-lines superimposed and in (b) galaxies from the V8k survey [26] as black dots with stream-lines superimposed. Courtesy of [27]

# 3 Illustris Dark-3 Simulation

The simulation data used is from the Illustris Dark-3[3] simulation (ILD3), full details of which can be found at the link above and in the footnote below. [23, 24]

## 3.1 What Universe are we in?

The initial conditions used in the simulation assume a $\Lambda$ Cold Dark Matter ($\Lambda$CDM) cosmology, where a dominant portion of the energy density of the Universe today comes from cold dark energy, in the form of the cosmological constant $\Lambda$. [2] According to [23, 24], and [28] this is consistent with observational data from the WMAP satellite.

As the simulation name suggests, it contains only dark matter (DM), providing a lighter computational load by modelling gravitation-only interactions of DM particles. It uses $455^3$ particles, with mass per particle of $4.8 \times 10^8$ [$M_\odot$], to resolve cosmic structure formation in a periodic volume of side-length $106.5$ [Mpc], with the cosmological parameters: $\Omega_m = 0.2726$, $\Omega_\Lambda = 0.7274$, $h = 0.704$, $H_0 = 100$ [hkms$^{-1}$], $n_s = 0.963$ and $\sigma_8 = 0.809$. [24] There are 136 snapshots available, with redshift values ranging from $z = 46.77$ to $z = 0.00$.

## 3.2 An initial look at the data

In order to get a qualitative understanding and intuition for the cosmic web and its evolution, some effort was devoted to visually analysing individual subhaloes and spatial sections of the simulation. This was done with the help of the illustris python package and API. On the right-hand side, in figure 9, is a high quality rendering from the illustris website of the dark matter density distribution.

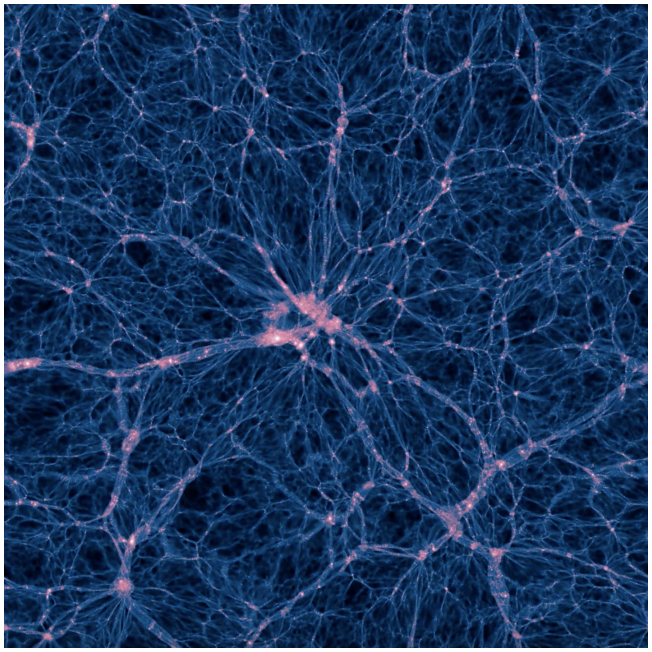

Figure 9: Dark matter density distribution slice at redshift 0 [23] [24]

### 3.2.1 Subhalo Analysis

According to anisotropic gravitational collapse theory, outlined in the previous section, it is to be expected that the general tendency of matter is to move out of underdense regions and into overdense ones. Further, we expect voids to get larger, as mass travels from them into nearby walls and filaments, finally reaching a node. Overall, the effect is that the unevenness of the landscape should increase with time because of these effects. To this end, a histogram plot was made of 2 of the three spatial

[3] Data from Illustris Dark-3 simulation is available at https://www.illustris-project.org/data/downloads/Illustris-3-Dark/

axes, projecting the frequency of particles present of the third axis.

Haloes are regions of space, dense in DM particles that are gravitationally bound together. Subhaloes are structures that remain distinct instead of merging to form larger haloes. The illustris API was especially useful in finding the largest subhaloes in the simulation at a given snapshot. Two directions were explored: finding the largest subhaloes at $z = 0.00$ and following them back in time to $z = 5.00$; and finding the largest subhaloes at $z = 5.00$ and following their evolution until $z = 0.00$. Due to the simulation resolution, the latter exploration did not yield much insight and will not be reported on. Following the identification of the largest subhaloes, a function was created that extracted the particle IDs within the subhalo, necessary for following them in time. Below are examples of histograms for the four largest subhaloes found at $z = 0.00$ that beautifully illustrate gravitational collapse. Animated gifs can be seen here.

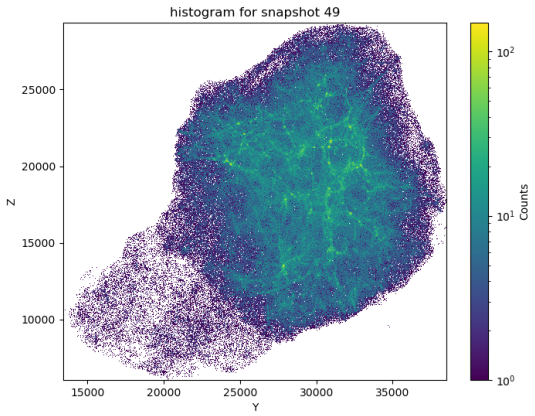


(a) Subhalo 0: snapshot 49 at $z = 5.00$

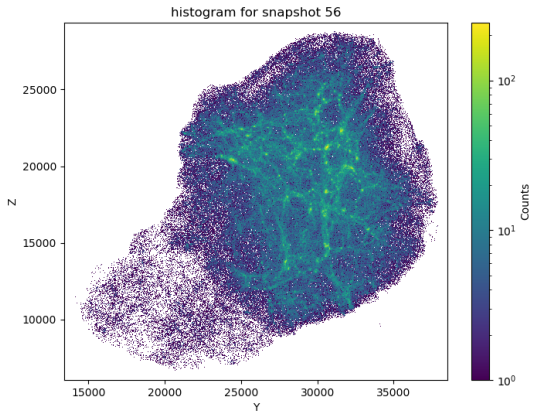


(b) Subhalo 0: snapshot 56, at $z = 3.71$

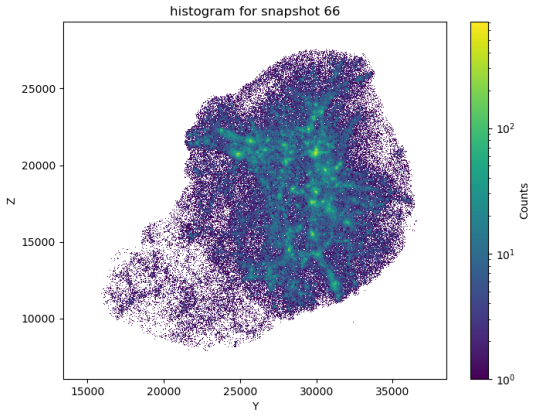


(c) Subhalo 0: snapshot 66, at $z = 2.21$

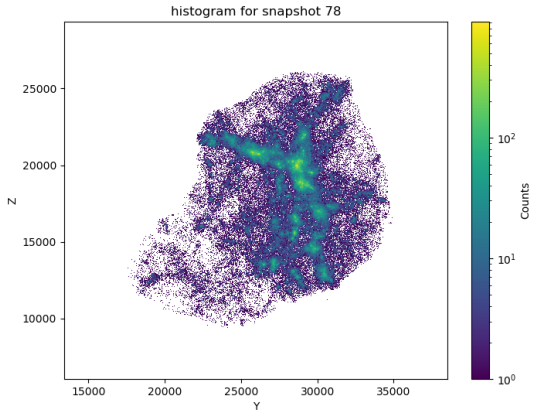


(d) Subhalo 0: snapshot 78, at $z = 1.30$

Figure 10: Subhalo 0 at several redshifts, highlighting gravitational collapse

Between the top panels in figure 10 we can see the subhalo structure becoming more prominent: nodes and voids alike are growing, with the ”Counts” scale (representing density) achieving a higher maximum value. In the bottom row panels we can observe a tendency towards a filamentary structure. The trend continues until the subhalo object that once presented intricate substructure collapses to

a filamentary region and ultimately ends up as a node. The histograms of the resulting node can be seen in the Appendices, in section A.1.

For purely visual motivations, let us examine subhalo 961. Besides the filamentary aspect of the mass density becoming more pronounced, this subhalo displays an interesting outer circular pattern that remains structurally intact almost throughout its entire evolution. Two other selected histograms of redshifts closer to $z = 0.00$ can be found in A.2

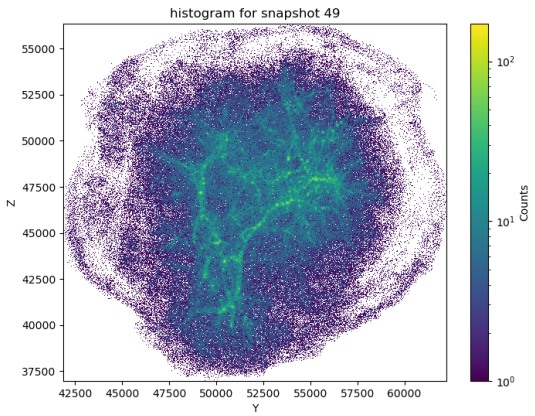


(a) Subhalo 961: snapshot 49 at $z = 5.00$

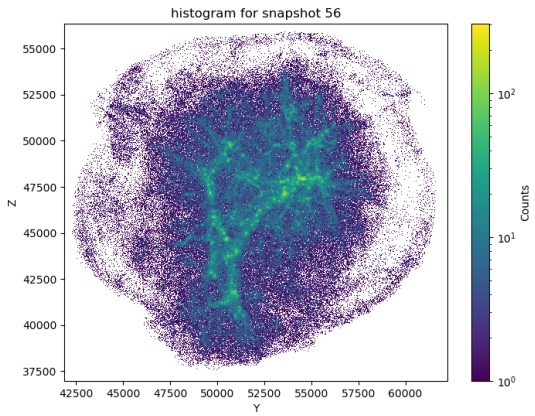


(b) Subhalo 961: snapshot 56, at $z = 3.71$

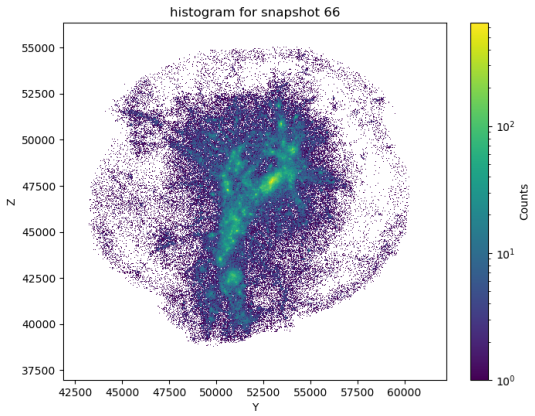


(c) Subhalo 961: snapshot 66, at $z = 2.21$

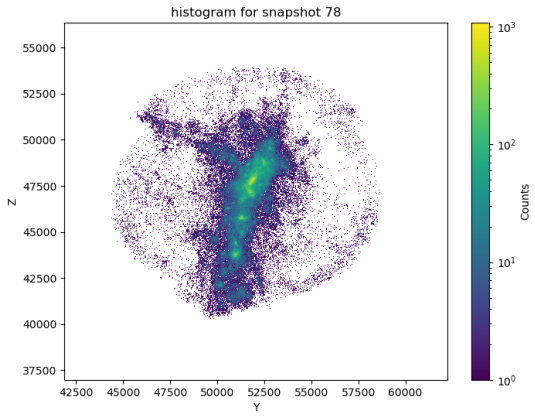


(d) Subhalo 961: snapshot 78, at $z = 1.30$

Figure 11: Subhalo 961 at several redshifts, highlighting mass transport

Similar changes can be observed for subhaloes 1890 and 574, which can be found in the Appendices, in sections A.3 and A.4, respectively.

### 3.2.2 Spatial Section Analysis

For spatial analysis the same two directions of analysis were undertaken: identify an area of interest at $z = 0.00$ and follow it back in time to $z = 4.66$ and the reverse (i.e. identify an interesting region at $z = 4.66$ and follow its evolution up til $z = 0.00$). Again, animated gifs of this process can be found here.

#### 3.2.2.a A node

In figure 12 we examine what looked like a node at $z = 0.00$. The number given to the node does not represent an ID of an object traceable back to illustris.

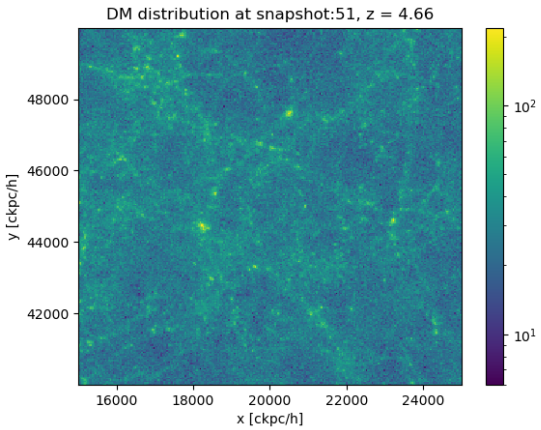


(a) node 1: snapshot 51 at $z = 4.66$

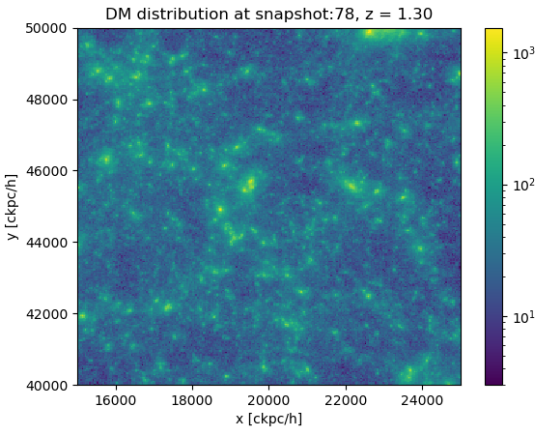


(b) node 1: snapshot 78, at $z = 1.30$

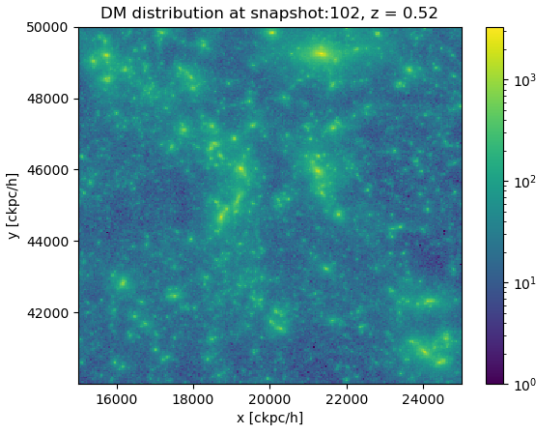


(c) node 1: snapshot 102, at $z = 0.52$

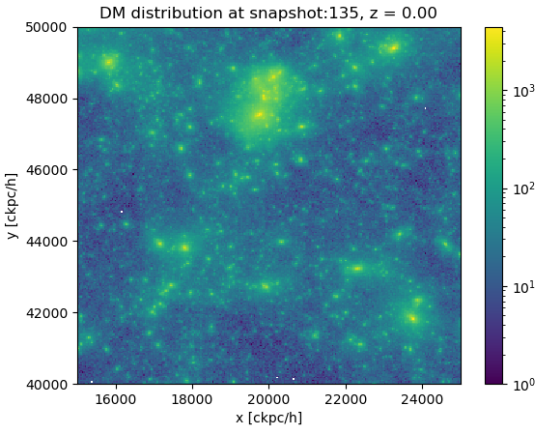


(d) node 1: snapshot 135, at $z = 0.00$

Figure 12: Node 1 at several redshifts

What is interesting here is that the node only makes its appearance in the region chosen around the snapshot 90, at $z = 0.85$ (it can be seen in the gif), indicating a strong gravitational pull from a nearby object.

#### 3.2.2.b A void region

In figure 13 we examine what looked like a void region at $z = 0.00$. Here the void number is not an ID that can be traced back to illustris, as in the previous section; the intention was to save the void from anonymity.

In the first image, top left panel, although not pronounced, we can already observe higher density in the ”outer” regions, save for the top right corner. The structures surrounding center therefore ”pull” the

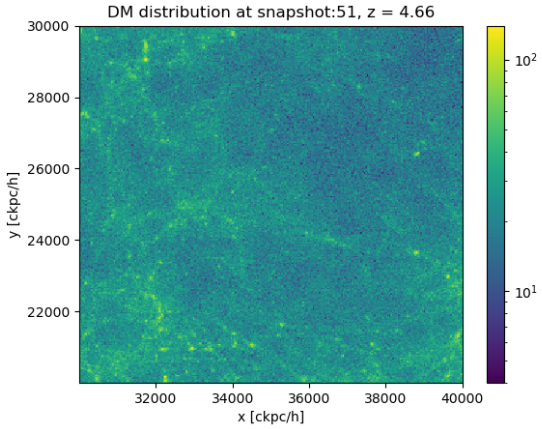


(a) void 1: snapshot 51 at $z = 4.66$

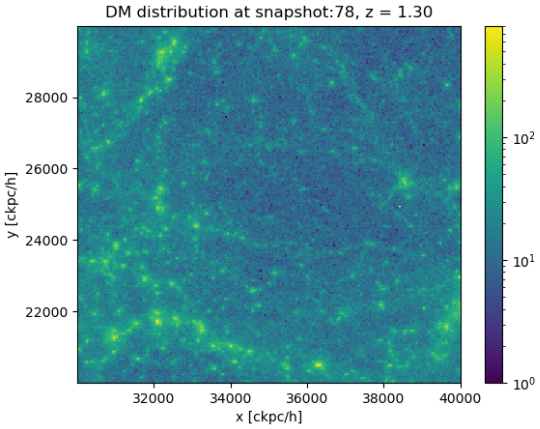


(b) void 1: snapshot 78, at $z = 1.30$

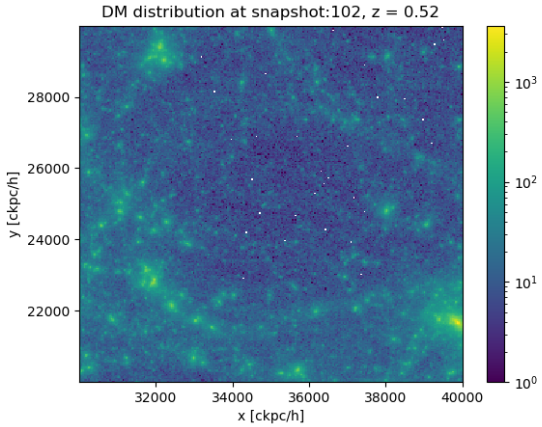


(c) void 1: snapshot 102, at $z = 0.52$

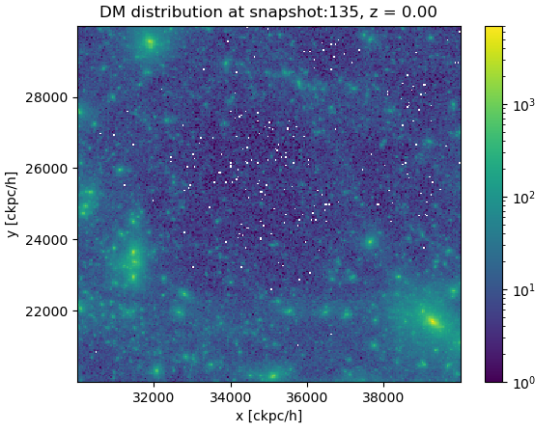


(d) void 1: snapshot 135, at $z = 0.00$

Figure 13: Void 1 at several redshifts, highlighting mass transport

mass towards themselves, leaving the middle region depleted in the bottom right hand panel. Another important aspect to observe in this final panel is the shot noise present. Because of the highly dense regions in the simulation data, the average density in a histogram bin is significant. Given that the shot noise expected is $\sigma_s = \sqrt{s}$, this implies that in highly underdense regions with very few particles present, there is a disproportionate amount of noise to signal ratio. **We fix this problem by using the DTFE method** which transforms the discrete distribution of points to a continuous field, as described in section 4.1.

#### 3.2.2.c Early filamentary region

To the bare eye, the area in figure 14 seemed to contain a filamentary region in snapshot 51, at $z = 4.66$. However, when zooming in on the region and plotting the evolution, it could not be determined clearly whether this was the case or not. Sight can provide a fantastic benchmark and give important insight, but examples such as this one highlight the need for objective methods of identification and quantification.

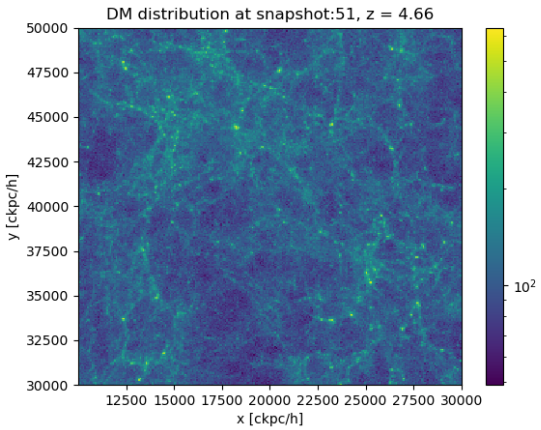


(a) filament 2: snapshot 51 at $z = 4.66$

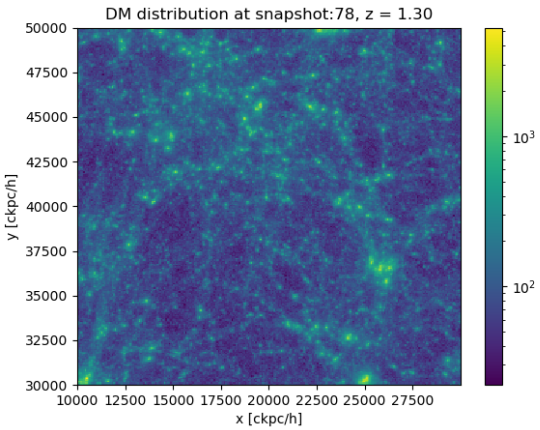


(b) filament 2: snapshot 78, at $z = 1.30$

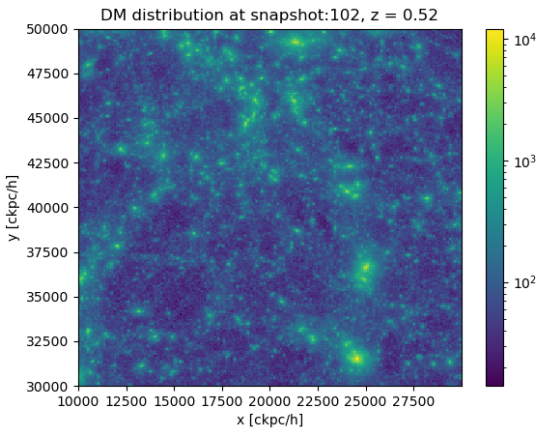


(c) filament 2: snapshot 102, at $z = 0.52$

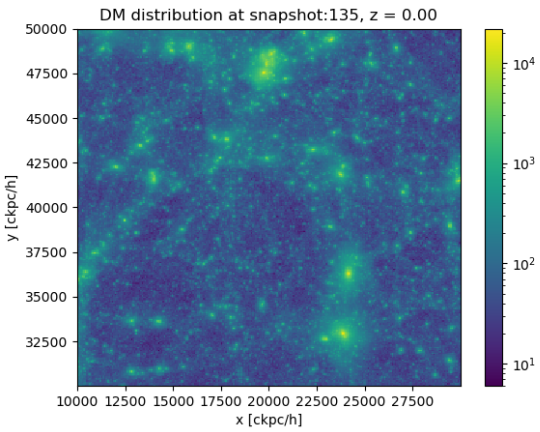


(d) filament 2: snapshot 135, at $z = 0.00$

Figure 14: Filament 2 at several redshifts, highlighting mass transport

# 4 Methods

We are looking to analyse mass transport throughout the environments of the Cosmic Web. In order to achieve this, initially ILD3 data had to be processed to obtain a density field. This was done with the Delaunay Tesselation Field Estimator (DTFE). [29][30][31] This is essential, as we use the resulting field as input the for NEXUS+ algorithm [7], which identified at each point in the field an environment type. More details about each program will be given in the following subsections, and some motivation for their suitability in tackling this analysis will be provided.

## 4.1 DTFE

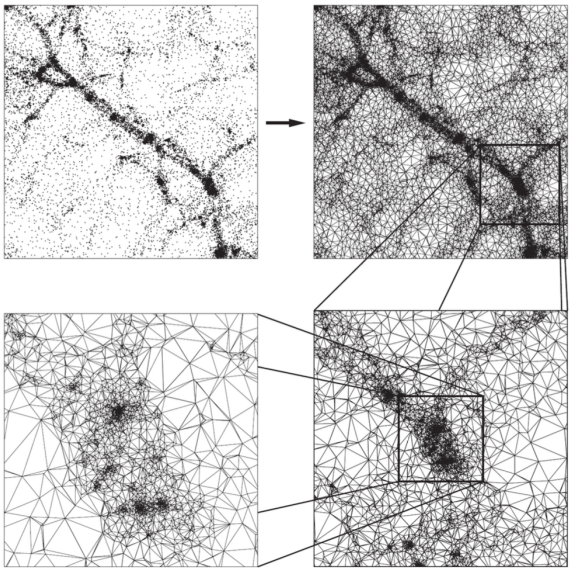

Figure 15: 2D DTFE from numerical simulation point set, taken from Schaap [32]

The DTFE method, introduced by Schaap and van de Weygaert in [30], is used to construct a continuous density and intensity field from a set of discrete points. As mentioned in section 3.2.2.b where a noisy void region was presented, this is paramount for better visualisation and understanding of the simulation data. Further, it is an imperative for later environment identification by NEXUS+. The program used in this thesis, built on that work, was developed by Marius Cautun [4].

There are several aspects of DTFE that make it so suitable for astrophysical data analysis. Firstly, the multi-scale aspect of the point distribution is preserved. This is especially important for cosmic structure simulations, where the density distribution varies over more than 6 orders of magnitude. Secondly, the local geometry of the point distribution is preserved, which allows for a detailed (high-resolution) image of the cosmic objects to be formed.[33] These aspects can be seen in figure 15, where a point distribution is plotted in the first box (upper left), the DTFE is plotted adjacent (upper right) and the subsequent images represent zoom-ins on a high-density region (lower left and right). By preserving the local geometry and multi-scale nature of the data, this method makes it possible to obtain high-resolution information that takes into account the hierarchically built structures found in the Cosmic Web, necessary for successful NEXUS+ characterisation of the web.

## 4.2 NEXUS+

To achieve an analysis of mass transport within the web, we need a method that can recognise structure objectively. This is challenging due to the complex pattern of the web- several types of morphological objects, intricately interconnected, exist at different scales and over a range of densities. A variety of methods have been developed to classify it; notable examples were categorised and

[4] The repository can be found here along with more details and a user guide

compared by Libeskind et al. Based on this classification, NEXUS is a "*Scale-space multiscale Hessian-based method*". An important aspect of this method, as the name suggests, is that it takes into account the multiscale nature of mass distribution observed in the web [25], without which characterisation of the web would be limited to a single smoothing scale. The method is versatile, in that it allows characterisation based on multiple fields: density, tidal, velocity divergence or velocity shear. The NEXUS+ method, found to better capture filamentary and wall structures [34] was used in this project.

NEXUS and NEXUS+ are programs built to elaborate on earlier work, the multiscale morphology filter (MMF) as presented by Aragón-Calvo et al. in [6]. The MMF algorithm was initially inspired by the work of Frangi et al. [35] and Sato et al. [36], from the field of medicine, specifically in detecting blood vessels in medical images. Given the complexity of patterns and multitude of scales and shapes in the vascular system, the knowledge could be translated and optimised to work on the similarly intricate and inter-connected structure of the web. By analysing local morphology as a function of scale (see figure 16), MMF managed to segment the cosmic web into its constituents automatically and in a scale-independent manner. As previously mentioned, this is paramount, given the hierarchical nature of evolution of mass which can be observed in the structure of the web.

The general NEXUS algorithm, as per [34], starts by applying a Gaussian filter on the input field, after which it computes the Hessian matrix eigenvalues. The smoothed field is given by:

$$f_{R_n}(\mathbf{x}) = \int \frac{d^3k}{(2\pi)^3} e^{-k^2 R_n^2/2} \hat{f}(\mathbf{k}) e^{i\mathbf{k}\cdot\mathbf{x}} \tag{4}$$

where $\hat{f}(\mathbf{k})$ is the Fourier transform of the input field $f(\mathbf{x})$ and $R_n$ is the width of the filter. The Hessian of the filtered field is found by:

$$\mathbf{H}_{ij,R_n}(\mathbf{x}) = R_n^2 \frac{\partial^2 f_{R_n}(\mathbf{x})}{\partial x_i \partial x_j} \tag{5}$$

where $\mathbf{H}_{ij,R_n}$ represents the i,j entry of the Hessian matrix. NEXUS makes use only of the eigenvalues of this matrix, given by the characteristic polynomial:

$$\det(\mathbf{H}_{ij,R_n}(\mathbf{x}) - \lambda_{a,R_n}(\mathbf{x})\delta_{ij}) = 0 \tag{6}$$

with the convention $\lambda_1 \leq \lambda_2 \leq \lambda_3$. Based on the eigenvalues determined, it assigns a signature (cluster, filament or wall) to each point[5], defined as:

$$S = I \times \begin{cases} |\lambda_3|\,\theta(-\lambda_1)\theta(-\lambda_2)\theta(-\lambda_3), & \text{cluster,} \\ |\lambda_2|\,\theta(-\lambda_1)\theta(-\lambda_2), & \text{filament,} \\ |\lambda_1|\,\theta(-\lambda_1), & \text{wall,} \end{cases} \tag{7}$$

where $\theta(x) = 1$ if $x \geq 0$ and 0 otherwise (i.e. the step function) and $I$ is the shape strength. This process is then repeated for a range of smoothing scales, thereby constructing a scale-space representation of the field (signatures of the points at different scales). By combining scale-space data, the most ample signature can be determined. Finally, a definitive and **scale-free** signature can be established by keeping in mind physical threshold detection criteria to validate the environments. [34] Similar to the segmentation according to eigenvalues in figure 4, NEXUS has the constraints shown in table 1.

[5] what is not found in the end to be contained in either one of these will be considered void

| Structure | Strict constraints |
|---|---|
| Cluster | $\lambda_1 < 0; \lambda_2 < 0; \lambda_3 < 0$ |
| Filament | $\lambda_1 < 0; \lambda_2 < 0$ |
| Wall | $\lambda_1 < 0$ |

Table 1: Hessian matrix eigenvalues associated to the different morphological components; constraints from expression 7, courtesy of [34]

NEXUS+ uses a log-Gaussian filter on the input field. Similarly to NEXUS:

$$g_{R_n}(\mathbf{x}) = \int \frac{d^3k}{(2\pi)^3} e^{-k^2 R_n^2/2} \hat{g}(\mathbf{k}) e^{i\mathbf{k}\cdot\mathbf{x}} \tag{8}$$

were $g = \log_{10} f$. This makes it attainable to create scale-space representations of the density field present in the web, which differs by several orders of magnitude from point to point. Without this additional method, the threshold value would have to be so low for NEXUS to distinguish some of the smaller filaments, that the larger filaments would be found to extend too far beyond their boundaries.[34]

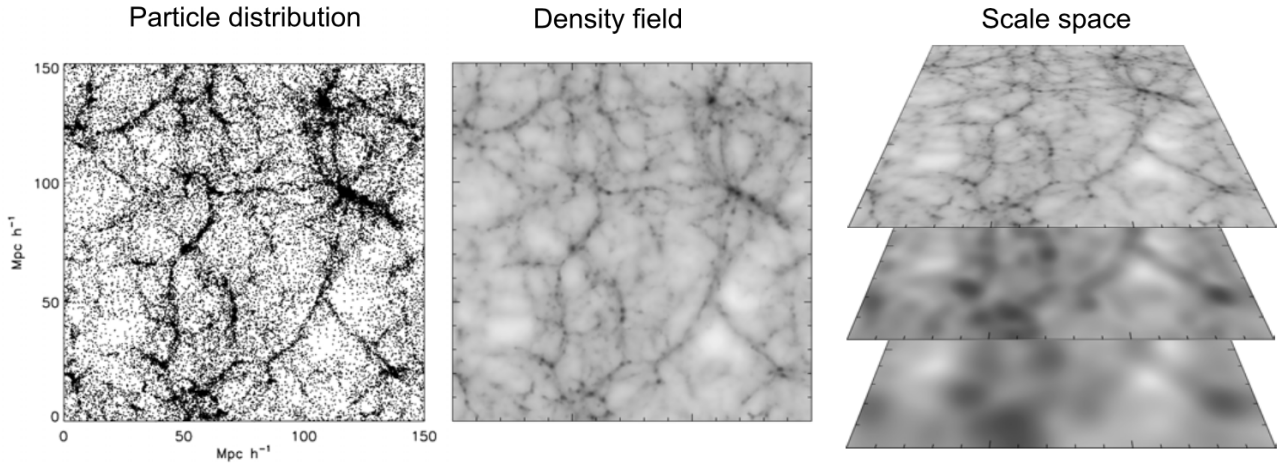


Figure 16: An example of how a particle distribution is transformed into a density field and ultimately into scale space representation, courtesy of [6]

## 4.3 Technical Note

While being the backbone of this project, these two **legacy programs** proved challenging to use and significant portions of the work undertaken for this project went into this aspect. Being written over 10 years ago in an older version of python, the syntax is different and they use deprecated packages to include inline C++ code in their python scripts. This meant that running a 2to3 command would not be enough to get scripts working. Another age-related issue was the file format system. When these were written, a now legacy ”format” designed specifically for snapshot data from cosmic simulations was commonly used - GADGET. The logic that portions of code use turned out to rely on the gadget formatting system[6].

[6]while it is true that the DTFE and therefore NEXUS+ would work with simple text files, this was not true for all the scripts necessary for completing the project

# 5 Mass Migration in the Web

We set out to identify the environments of the Cosmic Web in order to obtain an analysis of mass transport in the Cosmic Web. This would allow us to better understand how mass moves form one environment type to another, assembling to build up the large-scale web structure observed. To quantify this dynamic process, one requires the capacity to identify the environments in the web over a range of redshifts. As previously mentioned, NEXUS+ was used for this due to its scale-free identification capacity. To apply it to the discrete particle data-points of the simulation it was necessary to convert them to density fields that optimally retain the signal of anisotropic structures and their multi-scale embedding. This was done with the DTFE program, which ensures the retention of geometrical information and the multi-scale aspect of the point distribution. With these tools we are now ready to study mass transport in a quantitative way, as visualised in figures figs. 10 to 13, 14, 29 and 30.

## 5.1 Visual Identification

In this section we can finally take a look at the environments identified by the NEXUS+ MMF method. After obtaining a density field with he help of DTFE, NEXUS+ is able to identify the different types of environments found in the simulation box. As done previously, here we first use visualisation as a tool for gaining an initial perspective on the results. In figure 17 on the next page we can see, qualitatively,some results of the NEXUS+ MMF identification. The first panel, 17a, contains the density field used as input for NEXUS+, as output by DTFE. This will provide us with a visual benchmark for the performance of the identification method. In figures 17b, 17c and 17d we can observe the filaments, nodes and walls that were identified for the given density field respectively. Finally in figs. 17e and 17f we can see all identified object types superimposed, with the same colour encoding, respectively red contours for nodes, green contours for walls and blue contours for filaments. It should be noted that the particles not present in either one of these environment types are considered to be contained in a void region.

There is a clear match between what can be identified visually in the input density field and what was identified by NEXUS+, but we must remember here that the identification happens throughout the whole 3-dimensional box at once. Taking a slice will obscure to the eye the full information seen by NEXUS+ when classifying regions. Taking a slice of fixed z coordinates for plotting, we cannot see the vicinity of the region along the z-axis. For instance, in the upper left corner of the density field (17a), we may be tempted to visually identify the dense region around the point (9000,18750) as a node, but we can clearly see from figure 17b that in this particular slice it is part of a filament, which extends along the z-axis. This can be confirmed by comparing the two slices plotted in figures 17e and 17f, where we move along the z-axis from one panel to the other. We see that indeed there is a node nearby, connected to the identified filamentary region. To see more plots of identifications, please refer to the Appendix, section B. To see a gif of traversing the simulation cube with NEXUS+ identifications superimposed on the density field, please check the github repository.

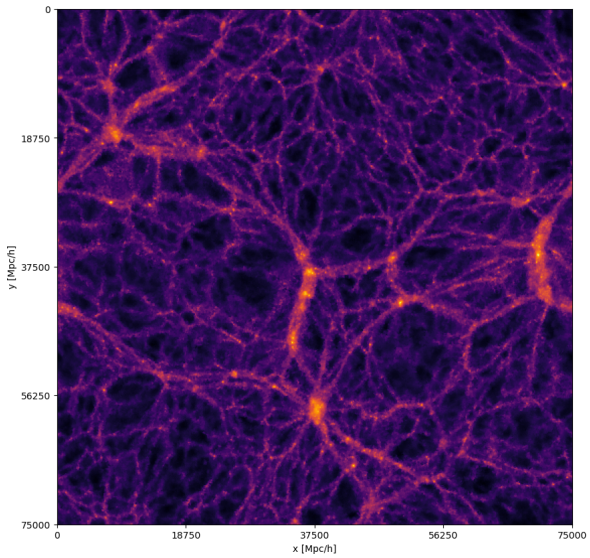


(a) DTFE density field at $z = 0.02$

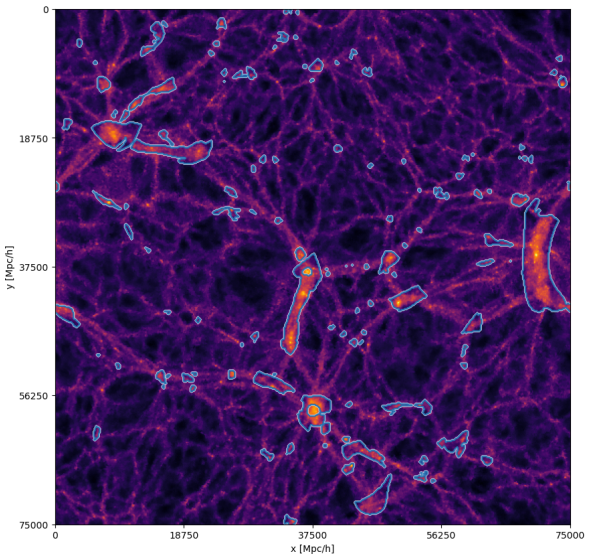


(b) NEXUS+ identified filaments at $z = 0.02$

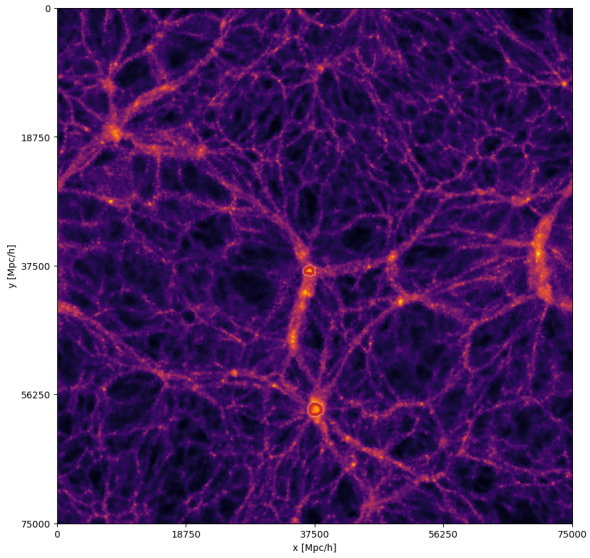


(c) NEXUS+ identified nodes at $z = 0.02$

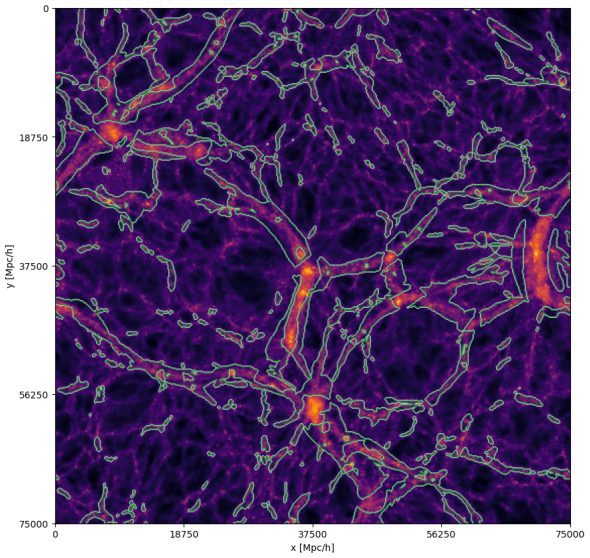


(d) NEXUS+ identified walls at $z = 0.02$

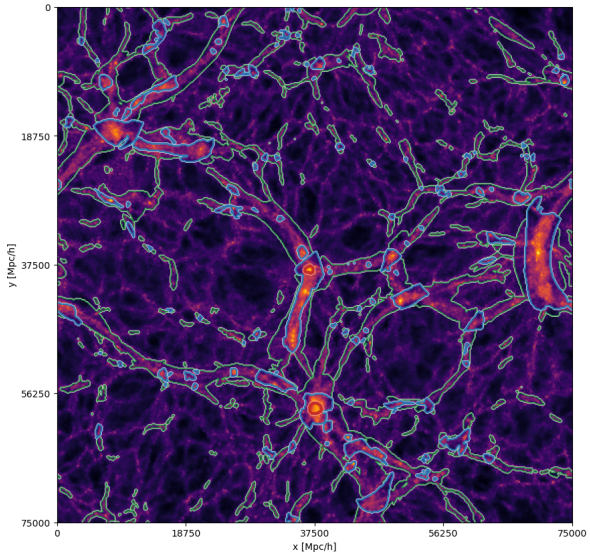


(e) NEXUS+ identified environments slice 0

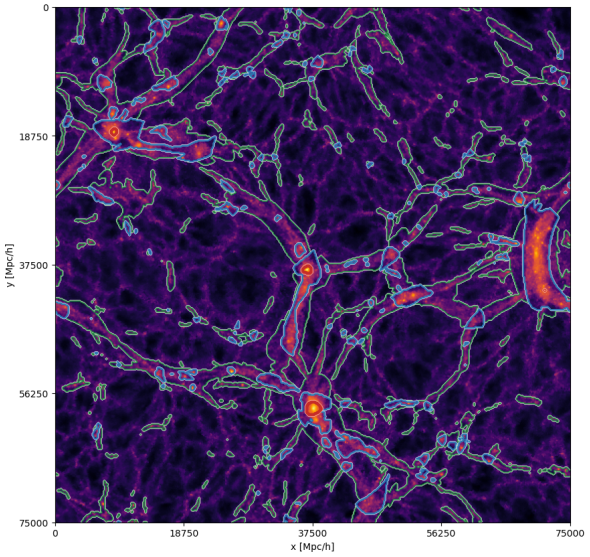


(f) NEXUS+ identified environments slice 2

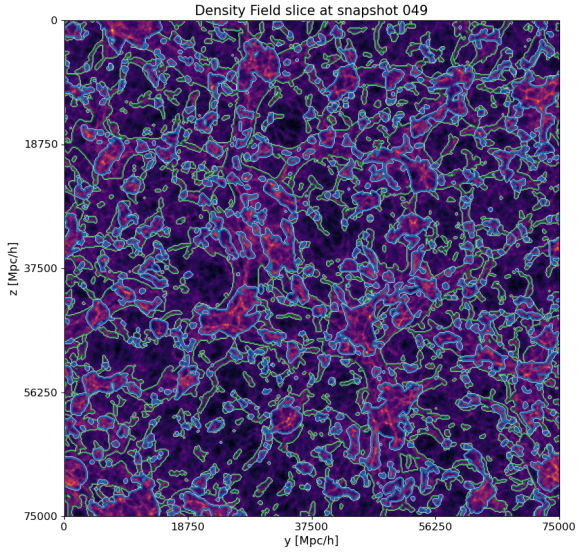


(a) Slice with NEXUS+ identifications at $z = 5.00$

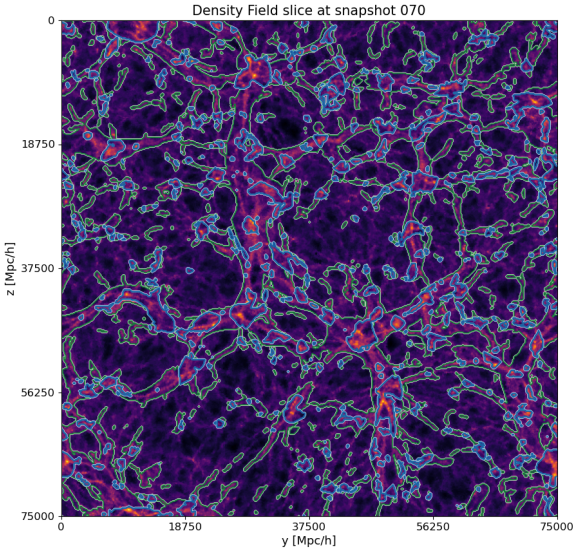


(b) Slice with NEXUS+ identifications at $z = 1.82$

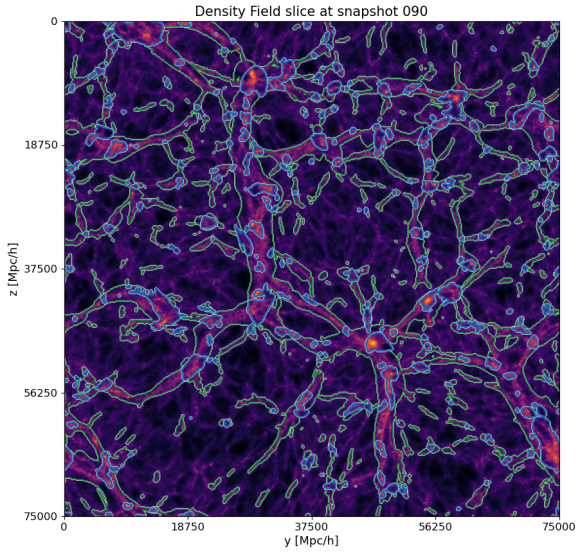


(c) Slice with NEXUS+ identifications at $z = 0.85$

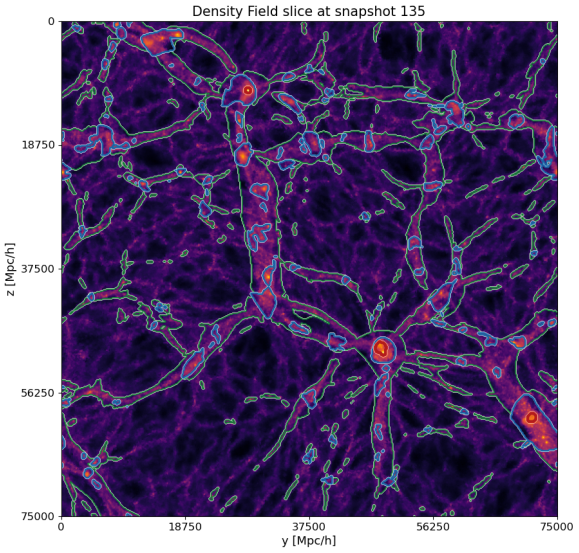


(d) Slice with NEXUS+ identifications at $z = 0.00$

Figure 18: NEXUS+ identifications of a slice, at varying redshifts

In order to get a better visual understanding of mass transports, we can fix a slice of the simulation and observe it at different redshifts. It would be highly recommended to pay a visit to the repository[7] for a moving gif of this, as it is far more beautiful and telling than static imagery. In figure 18 we can see an example of a slice at several redshifts. We can observe a somewhat uniform density distribution and lack of clusters in the primordial web, in panel 18a. As time passes we see structure start to emerge as mass clumps together in filamentary environments and eventually nodes, in panel 18d. Another

[7] https://github.com/diodeamy/Thesis/tree/main/ResultsPaper/gifs

slice example can be found in Appendix section B. Now that we have a better visual understanding of mass migration, we are finally ready to quantify it.

## 5.2 Quantifying Mass Transport

In this section we will look at how mass is transported across different morphological components in a quantitative manner. To quantify mass migration, I created a function to assign particle IDs to the respective environment in which the particle is found by NEXUS+, for each snapshot. Once we know for all snapshots in which type of object every particle is found, we can select all particles in a particular structure type at a specific snapshot, then extract the proportion of those particles found in each environment type, for the other snapshots. For more details about the procedure please refer to the Appendix section C. The procedure applied is directly equivalent to the common mass fraction, as defined by Cautun et al. [5]:

$$f_{ij}(z_1, z_2) = \frac{M_{(i;z_1)\cap(j;z_2)}}{M_{i;z_1}} \tag{9}$$

In equation 9 i and j represent types of environments, $z_1$ and $z_2$ represent redshifts, the numerator represents the overlap of mass in environment i at $z_1$ and the mass in environment j at $z_2$ and the denominator represents the mass in environment i at $z_1$. This is a very useful way to formulate the problem because if we select:

- $z_1 > z_2$: the fraction represents the fraction of $z_1$ mass in environment i, that can be found in environment j at a later $z_2$
- $z_1 < z_2$: the fraction represents the amount of mass in environment i at $z_1$ that originated in environment j at $z_2$

With this in mind we can examine the history of today's environments, as well as the evolution of environments from $z = 5.00$.

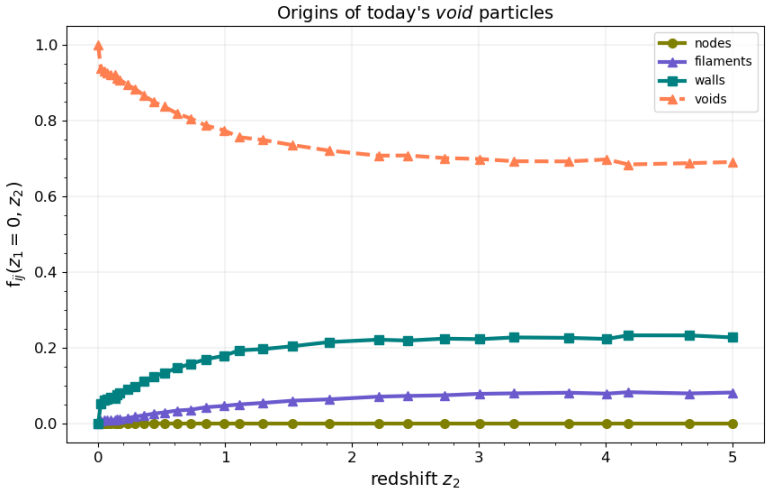


Figure 19: Origins of void particles; common mass fraction as a function of redshift $z_2$

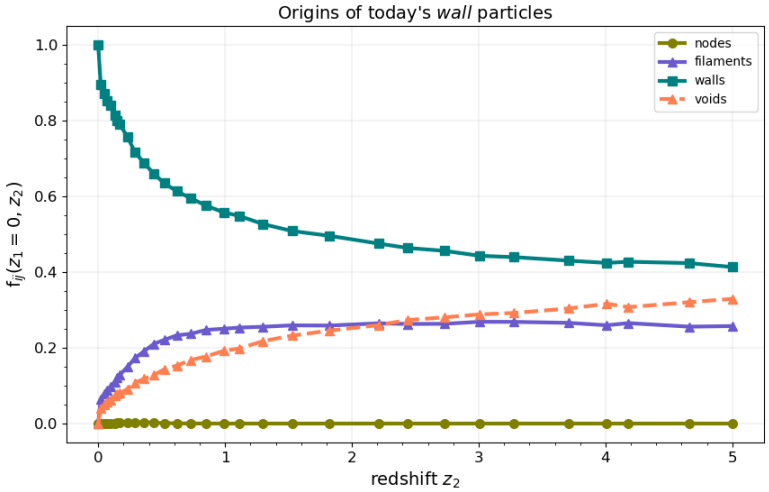


Figure 20: Origins of wall particles; common mass fraction as a function of redshift $z_2$

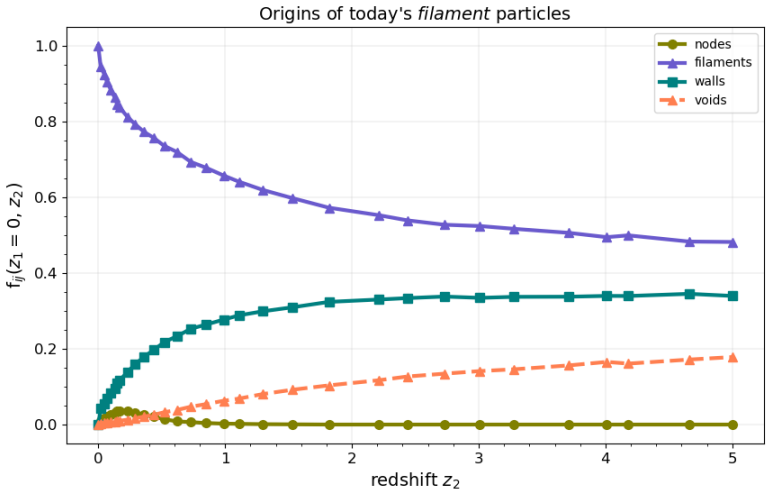


Figure 21: Origins of filament particles; common mass fraction as a function of redshift $z_2$

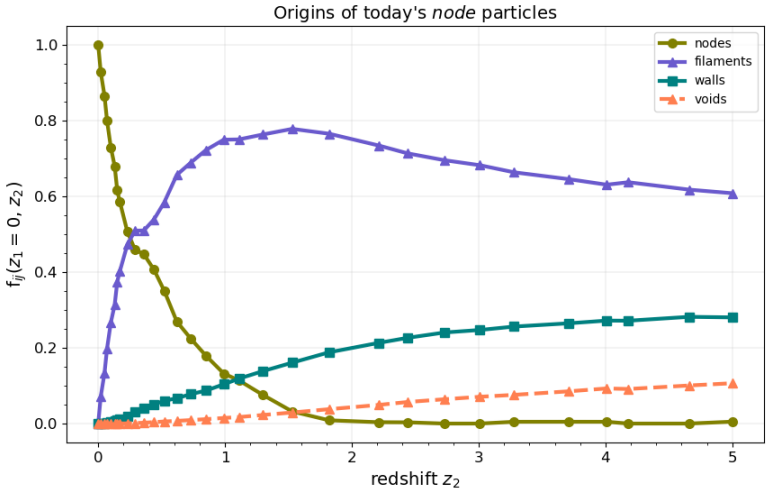


Figure 22: Origins of node particles; common mass fraction as a function of redshift $z_2$

In figs. 19 to 22 we can see the results of this operation, when picking today as a base snapshot ($z_1 = 0.00$) and looking back as far as $z_2 = 5.00$. Plotted for each environment type is the common mass fraction, as a function of the varying redshift $z_2$. For each particle that was in a void, node, filament or wall at $z = 0.00$, we can see at different redshifts what other environment it was in. This allows us to essentially look at the history of today's environments, tracing their particles back in time to quantify the proportion of environment types they were found in at different redhsifts.

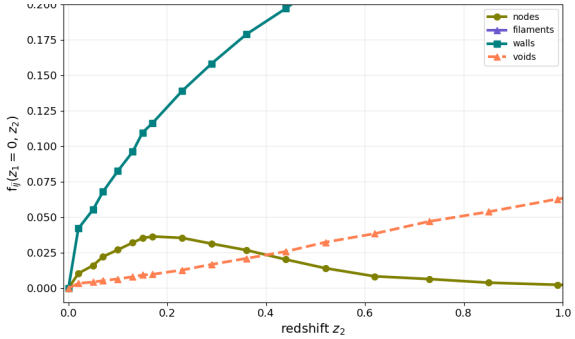


Figure 23: Peculiar increase in proportion of node particles

Based on the Zel'dovich formalism for anisotropic gravitational collapse, outlined in section 2, we expect to see a clear pattern of mass migration: particles move from voids to walls, then to filaments, finally ending up in nodes. It can be immediately seen that this is not entirely in accord with the results. In figure 19 we observe that around 20% of particles in today's voids were in walls and around 10% were in filaments until approximately $z_2 = 1.00$, in clear contradiction with the mass flow predicted. The same can be said for figure 20 where we notice that around 25% of wall particles started out in filaments at $z = 5.00$. As argued by Cautun et al., this is indicative of the limitations of NEXUS+. The authors conclude that the errors are due to incorrect or incomplete identification of particles from underdense regions.[5] Still, the results in figure 22 seem to agree well with the theoretical prediction since most of their mass originated in filaments. In figure 21 we see that most most of today's filament mass was either already in filamentary environments, or migrated from walls, also agreeing with the standard picture. Around a redshift of $z_2 = 0.40$ something curious happens in figure 21- it appears that there is a sudden inflow of particles into nodes. This can be inspected closer in figure 23.

A possible explanation for this phenomenon may involve particles moving from walls and voids into regions identified as nodes. These particles were likely "just passing through" these node areas on

their way to a filament structure, to which they were gravitationally bound. Alternatively, it could indicate some large filaments temporarily overlapping amidst a larger-scale movement and being identified as nodes. Subsequently, they would be appropriately identified as filament particles. It is unlikely that this is a global phenomenon, and probably has to do with the NEXUS+ identification.

Around the same redshift ($z = 0.40$), in figure 22 a sharp decrease of transport from filaments to nodes can be observed. This pattern may align with the previously discussed increase in filament transport into nodes. There is a clear general trend of heightened migration from filaments into nodes at these redshifts. The overlap of two large filamentary structures suddenly identified as nodes, which would momentarily increase the filament-to-node ratio, could be obscured by this. While most filament particles would continue flowing to nodes, these specific filaments would revert to being ”appropriately” classified as filaments, potentially causing the observed stagnation.

In figs. 24 to 26 the reverse process can be observed, particularly we observe how mass is transported from environments as time passes, by picking $z_1 = 5.00$ as a base snapshot and following the mass until today at $z_2 = 0.00$. Plotted for each environment type is the common mass fraction, as a function of the varying redshift $z_2$.

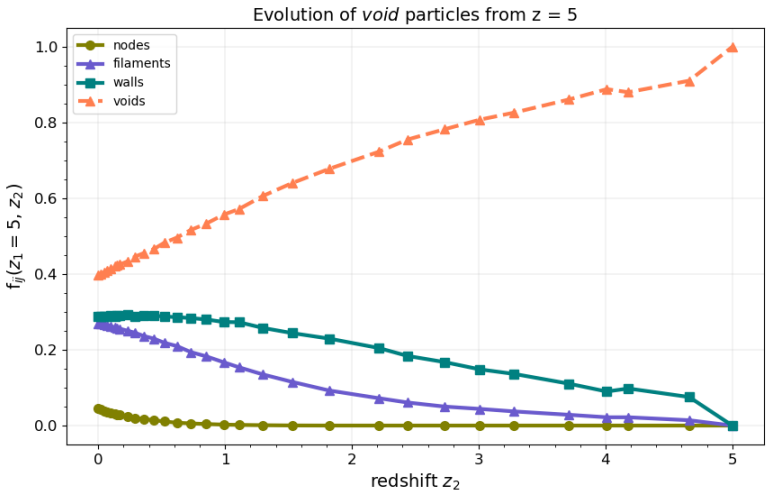


Figure 24: Environments of origin of voids at $z = 5.00$

It should be noted why there is no such figure for the nodes identified. When running NEXUS+ a certain threshold value for what is to be considered a node must be selected. This was done at all snapshots with the value of $5 \times 10^{13}$ in units of $[M_\odot/h]$ (determined by [34] as the appropriate cluster signature); it naturally means that at early redshifts, there simply will not be any objects in the simulation that fit this criteria given the more uniform primordial density field which lacks such massive clusters, as was shown in the panel 18a. This implies that the algorithm has a hard time assigning appropriate environment signatures, and very few nodes are identified. It can be seen from figure 24 and 25 that mass quickly flows out of wall and void environments. Only around 40% of void mass remains in void environments and about 35% of wall particles are still contained in walls at present. This shows significant mass flow from underdense regions, as was predicted. Further, it could be noted that in figure 25 we only see around 15% of particles traveling ”the wrong way” (moving from walls into voids)

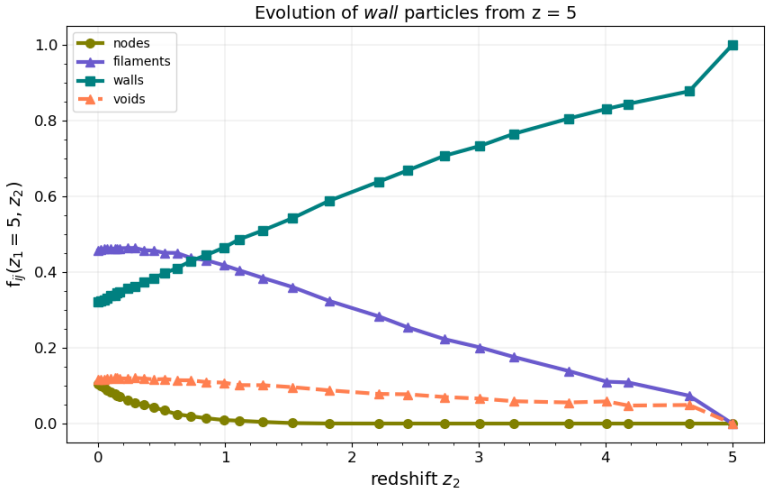


Figure 25: Environments of origin of walls at $z = 5.00$

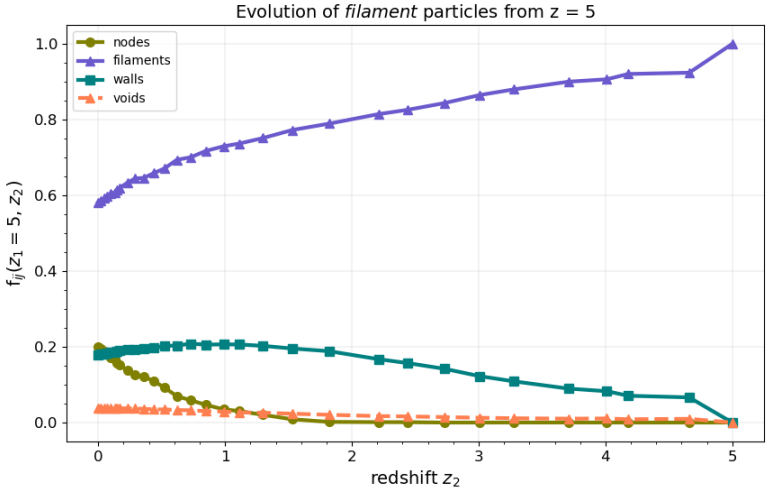


Figure 26: Environments of origin of filaments at $z = 5.00$

and in figure 26 around 20% of filaments relocating from filaments into walls.

In conclusion, in the visual representations of mass flow the expected pattern clearly emerges: mass migrates away from underdense void regions, and these become larger with time. Mass can be seen moving into the more dense regions. Since walls are at the boundaries of void regions, it is natural that particles first migrate there, before making their way into the filaments that connect them. It can then be observed that the density field presents the tendency of clumping up at the meeting points of filaments, creating overly dense clusters of mass. This structure becomes more and more pronounced with time until finally, voids take up most of the space and nodes and filaments contain most of the mass available. Also in the common mass fraction plots we can observe general agreement with the predicted outcome, as most particles migrate to their foreseen environments. As the authors outline in the paper describing the NEXUS+ method [5], the discrepancies found are likely due to the misidentification of environments in very low density areas.

# 6 Conclusion

In this thesis, I set out to study the intricate process that shape the Cosmic Web- how initial perturbations in an almost uniform primordial field created a runaway process where mass flows into the slightly denser regions and out of the less dense regions; and how local mass arrangements dictate the deformation of the space they occupy, ultimately deciding whether its fate is to inhabit a void, wall, filament or cluster. The anisotropic nature of gravitational collapse happening over a multitude of scales, coupled with mass flows, have created the web structure. Given enough time, this structure once characterised by linear fluctuations evolved into the intricate nonlinear web structure that weaves together our space.

The investigation into the dynamics of mass transport, from proto-structure to present times, has provided significant insights into the process of cross-environment mass migration. Using simulation data allowed us to ”experimentally” examine this process at much larger redshift values than is currently possible by observation. By using DTFE in conjecture with the NEXUS+ MMF program we were able to characterise the data from the ILD3 simulation. It was possible due to the capability of the two programs to preserve essential characteristics of the density distribution contained in the points to be maintained, specifically the local morphology and multi-scale, hierarchical nature of the Cosmic Web.

The predicted sequence of mass flows, based on the Zel’dovich approximation, is that mass should flow from voids into the surrounding walls, after which they are transported along filaments into nodes. The visualisation made clearly showed this tendency and when quantifying mass transport, the results aligned quite well with this prediction as well. While some discrepancies were found between the observed and predicted mass flows, these are most likely due to erroneous characterisation by NEXUS+ in underdense regions. We could therefore conclude that the general agreement of results reinforce the validity of the theoretical framework.

In order to fully understand the phenomenon of mass transport across different web environments, a more in depth analysis could be undertaken in the future- one that would include observing the velocity fields of the data. As the main driver of mass flow, the peculiar velocity field would potentially give conclusive evidence of the sequence of mass migration to different morphological components and would be comparable to the graphs obtained by observational data studies (such as the ones shown in figure figs. 7 and 8).

To conclude, the study of the Cosmic Web is a journey into the heart of cosmology itself. It reveals to us the processes that have shaped our Universe from its inception to its present day state, providing a framework for future discoveries[8].

[8]Some further questions linger on my mind after completing this analysis: (1) Is it possible that particles simply remain in their respective environment, never flowing to a different morphological structure? (this could be, in principle, tested already from the present results), (2) Could we find the precise reason for the peculiarities in the node-filament graphs discussed in the Results section?, (3) If anisotropic gravitational collapse happens at a multitude of scales, where are the limits of this? Will it be fractal in nature, extending into the realm of quantum foam for instance? Could we infer from its properties anything about the nature quantum foam?

## 6.1 Historical Context

Since at least the time of the ancient Assyro-Babilonians in 1000 BC , humankind has been keeping detailed records of the motion of planets beyond our own.[37] At first this may have only served a utilitarian purpose: track planetary and star motion and you can track time itself. This would aid in agriculture, navigation and even religious rituals. Hundreds of years passed before Greek astronomers attempted to use this information to determine cosmic scales, and heliocentricity was proposed by Aristarchus of Samos in the third century BC. [38] With the fall of the Greek empire and the decay of the library of Alexandria, astronomy continued to flourish predominantly in Asia and in the Islamic world until the European region woke up from the Dark Ages. With the invention of the telescope in the Netherlands in 1608, fundamental discoveries were made possible: evidence was found to support Copernicus's heliocentric theory and with Galileo's observations and Kepler's laws of planetary motion, Newton was inspired to write his general theory of gravity.

Colonial powers, like the French and English empires, were motivated to create precise sky-maps for navigation and established two great observatories (at Paris and Greenwich respectively). It was here that mounting evidence presented itself to support the fact that astronomical distances are enormous- Cassini's estimate of the distance to Mars allowed an estimate of the entire Solar System- and that Halley compared these sky catalogues to ancient Greek ones to show that stars are not fixed, but move through space. As more precise measurements became reality, bolder theories became testable and the limits of human imagination moved farther and farther out, even beyond the observable[9]. One can speculate that since the beginning, humans have pondered questions bigger than them: where do we come from? how, when and from what did everything appear? how will it all end? For the first time the history of humankind, we have a real chance of answering these questions. What started out as a utilitarian stride has given us one of the most fascinating and awe-inducing branches of modern-day science: cosmology. The ball is in our court.

[9] for instance quantum theory and anything before the CMB

# Bibliography

[1] F.-S. Kitaura, P. Erdogdu, S. E. Nuza, A. Khalatyan, R. E. Angulo, Y. Hoffman, and S. Gottloeber, "Cosmic structure and dynamics of the local universe," 5 2012.

[2] B. Ryden, *Introduction to Cosmology*. Cambridge University Press, 11 2016.

[3] J. R. Bond, L. Kofman, and D. Pogosyan, "How filaments of galaxies are woven into the cosmic web," *Nature*, vol. 380, pp. 603–606, 4 1996.

[4] R. van de Weygaert and J. R. Bond, *Clusters and the Theory of the Cosmic Web*, pp. 335–408. 2008.

[5] M. Cautun, R. van de Weygaert, B. J. T. Jones, and C. S. Frenk, "Evolution of the cosmic web," *Monthly Notices of the Royal Astronomical Society*, vol. 441, pp. 2923–2973, 7 2014.

[6] M. A. Aragon-Calvo, B. J. T. Jones, R. van de Weygaert, and J. M. van der Hulst, "The multiscale morphology filter: Identifying and extracting spatial patterns in the galaxy distribution," 5 2007.

[7] M. Cautun, R. van de Weygaert, B. J. T. Jones, C. S. Frenk, and W. A. Hellwing, "Nexus of the cosmic web," 11 2012.

[8] NOIRLab, "Desi year-one data slice." `https://noirlab.edu/public/images/noirlab2408b/`. Accessed: 2010-09-30.

[9] P. J. E. Peebles, *The large-scale structure of the universe*. 1980.

[10] J. M. Colberg, K. S. Krughoff, and A. J. Connolly, "Intercluster filaments in a cdm universe," *Monthly Notices of the Royal Astronomical Society*, vol. 359, pp. 272–282, 5 2005.

[11] V. Springel, S. D. M. White, A. Jenkins, C. S. Frenk, N. Yoshida, L. Gao, J. Navarro, R. Thacker, D. Croton, J. Helly, J. A. Peacock, S. Cole, P. Thomas, H. Couchman, A. Evrard, J. Colberg, and F. Pearce, "Simulations of the formation, evolution and clustering of galaxies and quasars," *Nature*, vol. 435, pp. 629–636, 6 2005.

[12] J. Shen, T. Abel, H. J. Mo, and R. K. Sheth, "An excursion set model of the cosmic web: The abundance of sheets, filaments, and halos," *The Astrophysical Journal*, vol. 645, pp. 783–791, 7 2006.

[13] K. Dolag, M. Meneghetti, L. Moscardini, E. Rasia, and A. Bonaldi, "Simulating the physical properties of dark matter and gas inside the cosmic web," *Monthly Notices of the Royal Astronomical Society*, vol. 370, pp. 656–672, 8 2006.

[14] B. Moore, F. Governato, T. Quinn, J. Stadel, and G. Lake, "Resolving the structure of cold dark matter halos," *The Astrophysical Journal*, vol. 499, pp. L5–L8, 5 1998.

[15] M. Davis, G. Efstathiou, C. S. Frenk, and S. D. M. White, "The evolution of large-scale structure in a universe dominated by cold dark matter," *The Astrophysical Journal*, vol. 292, p. 371, 5 1985.

[16] S. D. M. White, C. S. Frenk, M. Davis, and G. Efstathiou, "Clusters, filaments, and voids in a universe dominated by cold dark matter," *The Astrophysical Journal*, vol. 313, p. 505, 2 1987.

[17] R. K. Sheth and R. van de Weygaert, "A hierarchy of voids: much ado about nothing," *Monthly Notices of the Royal Astronomical Society*, vol. 350, pp. 517–538, 5 2004.

[18] J. V. Sheth, "Morphology of mock sdss catalogues," *Monthly Notices of the Royal Astronomical Society*, vol. 354, pp. 332–342, 10 2004.

[19] H. M. Courtois, D. Pomarede, R. B. Tully, Y. Hoffman, and D. Courtois, "Cosmography of the local universe," 6 2013.

[20] C. Raeth, A. J. Banday, G. Rossmanith, H. Modest, R. Suetterlin, K. M. Gorski, J. Delabrouille, and G. E. Morfill, "Scale-dependent non-gaussianities in the wmap data as identified by using surrogates and scaling indices," 12 2010.

[21] J. M. Bardeen, J. R. Bond, N. Kaiser, and A. S. Szalay, "The statistics of peaks of gaussian random fields," *The Astrophysical Journal*, vol. 304, p. 15, 5 1986.

[22] Y. B. Zel'dovich, "Gravitational instability: An approximate theory for large density perturbations.," *Astronomy and Astrophysics*, vol. 5, pp. 84–89, 3 1970.

[23] D. Nelson, A. Pillepich, S. Genel, M. Vogelsberger, V. Springel, P. Torrey, V. Rodriguez-Gomez, D. Sijacki, G. F. Snyder, B. Griffen, F. Marinacci, L. Blecha, L. Sales, D. Xu, and L. Hernquist, "The illustris simulation: Public data release," 4 2015.

[24] M. Vogelsberger, S. Genel, V. Springel, P. Torrey, D. Sijacki, D. Xu, G. F. Snyder, S. Bird, D. Nelson, and L. Hernquist, "Properties of galaxies reproduced by a hydrodynamic simulation," 5 2014.

[25] N. I. Libeskind, R. van de Weygaert, M. Cautun, B. Falck, E. Tempel, T. Abel, M. Alpaslan, M. A. Aragón-Calvo, J. E. Forero-Romero, R. Gonzalez, S. Gottlöber, O. Hahn, W. A. Hellwing, Y. Hoffman, B. J. T. Jones, F. Kitaura, A. Knebe, S. Manti, M. Neyrinck, S. E. Nuza, N. Padilla, E. Platen, N. Ramachandra, A. Robotham, E. Saar, S. Shandarin, M. Steinmetz, R. S. Stoica, T. Sousbie, and G. Yepes, "Tracing the cosmic web," *Monthly Notices of the Royal Astronomical Society*, vol. 473, pp. 1195–1217, 1 2018.

[26] R. B. Tully, L. Rizzi, E. J. Shaya, H. M. Courtois, D. I. Makarov, and B. A. Jacobs, "The extragalactic distance database," 2 2009.

[27] N. I. Libeskind, Y. Hoffman, R. B. Tully, H. M. Courtois, D. Pomarède, S. Gottlöber, and M. Steinmetz, "Planes of satellite galaxies and the cosmic web," *Monthly Notices of the Royal Astronomical Society*, vol. 452, pp. 1052–1059, 9 2015.

[28] J. Primack, "Historical introduction to cdm cosmology."

[29] R. van de Weygaert and W. Schaap, "The cosmic web: Geometric analysis," 8 2007.

[30] W. E. Schaap and R. van de Weygaert, "Continuous fields and discrete samples: Reconstruction through delaunay tessellations," 11 2000.

[31] M. C. Cautun and R. van de Weygaert, "The dtfe public software: The delaunay tessellation field estimator code," 5 2011.

[32] W. E. Schaap, "Dtfe: the delaunay tessellation field estimator," 2007.

[33] M. Cautun, “User guide for dtfe,” 2011.

[34] M. Cautun, R. van de Weygaert, and B. J. T. Jones, “Nexus: tracing the cosmic web connection,” *Monthly Notices of the Royal Astronomical Society*, vol. 429, pp. 1286–1308, 2 2013.

[35] A. F. Frangi, W. J. Niessen, K. L. Vincken, and M. A. Viergever, *Multiscale vessel enhancement filtering*, pp. 130–137. 1998.

[36] Y. Sato, S. Nakajima, N. Shiraga, H. Atsumi, S. Yoshida, T. Koller, G. Gerig, and R. Kikinis, “Three-dimensional multi-scale line filter for segmentation and visualization of curvilinear structures in medical images,” *Medical Image Analysis*, vol. 2, pp. 143–168, 6 1998.

[37] E. S. Agency, “A history of astrometry - part i mapping the sky from ancient to pre-modern times.”

[38] wiki commons, “Aristarchus of samos.”

# Appendices

## A More Subhalo Figures

In this section we can see the additional images of the subhalo analyses from section 3, particularly two final snapshots of subhalos 0 and 961 in section A.1 and section A.2 respectively; and the plots showing the ”entire” collapse of subhalos 1890 and 574 in section A.3 and section A.4 respectively.

### A.1 Subahlo 0

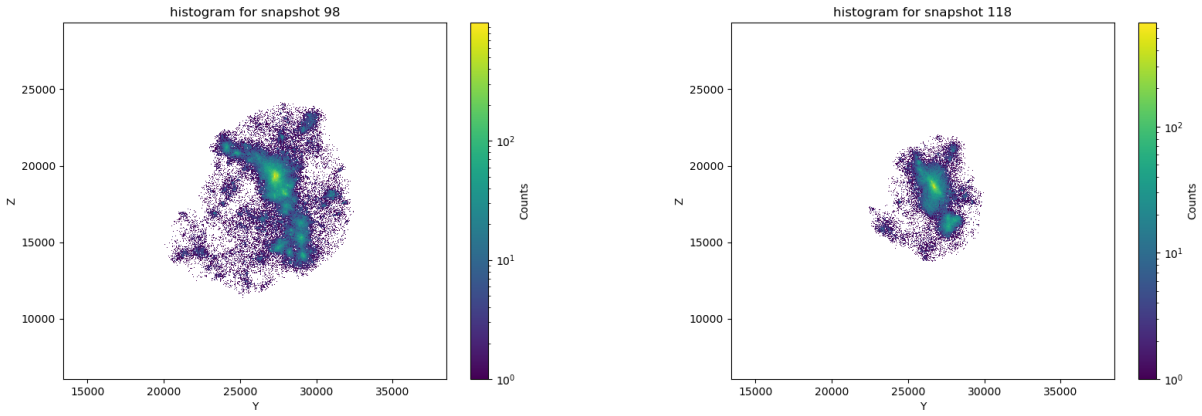


(a) Subhalo 0: snapshot 98, at $z = 0.62$

(b) Subhalo 0: snapshot 118, at $z = 0.23$

Figure 27: Subhalo 0 turning from filament to node

### A.2 Subhalo 961

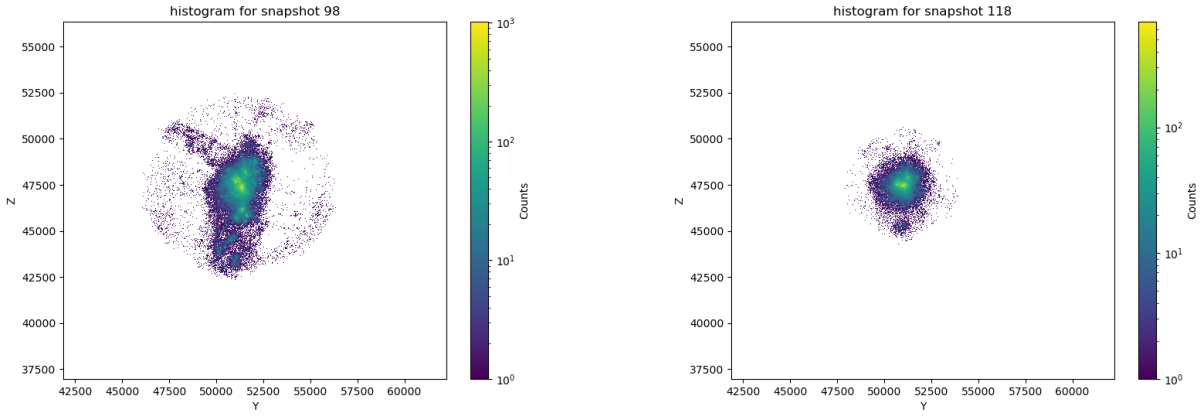


(a) Subhalo 961: snapshot 98, at $z = 0.62$

(b) Subhalo 961: snapshot 118, at $z = 0.23$

Figure 28: Subhalo 961 at two more redshifts

## A.3 Subhalo 1890

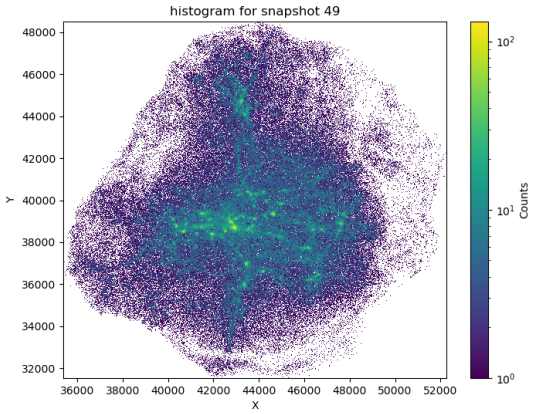


(a) Subhalo 1890: snapshot 49 at $z = 5.00$

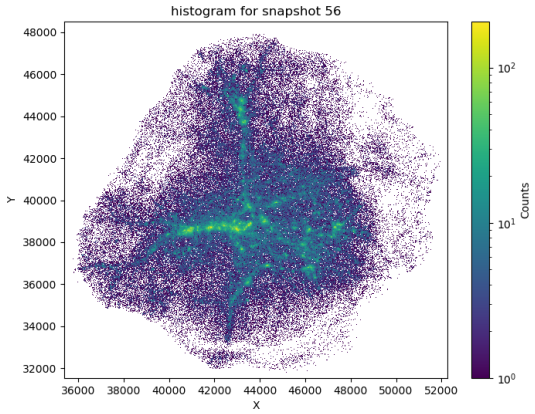


(b) Subhalo 1890: snapshot 56, at $z = 3.71$

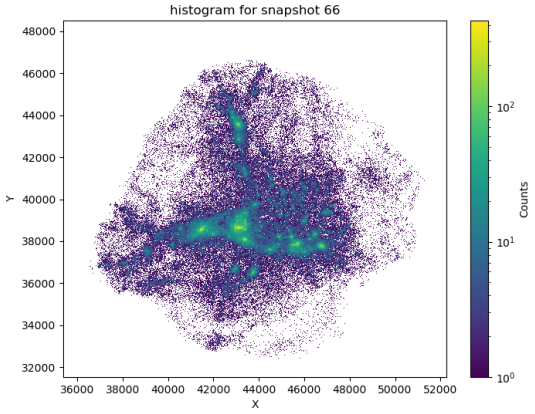


(c) Subhalo 1890: snapshot 66, at $z = 2.21$

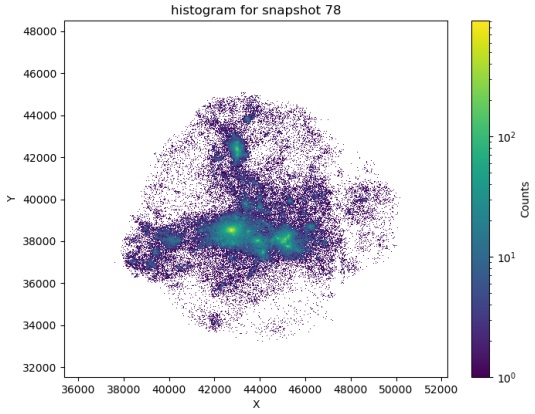


(d) Subhalo 1890: snapshot 78, at $z = 1.30$

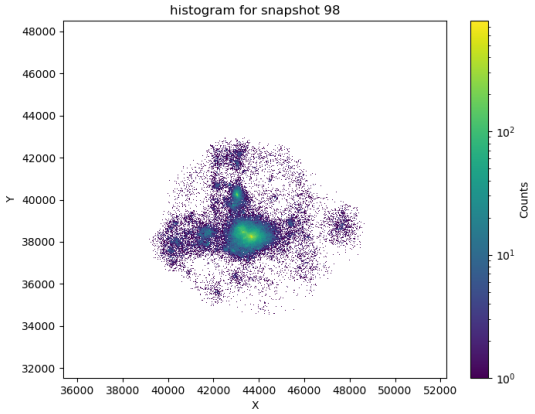


(e) Subhalo 1890: snapshot 98, at $z = 0.62$

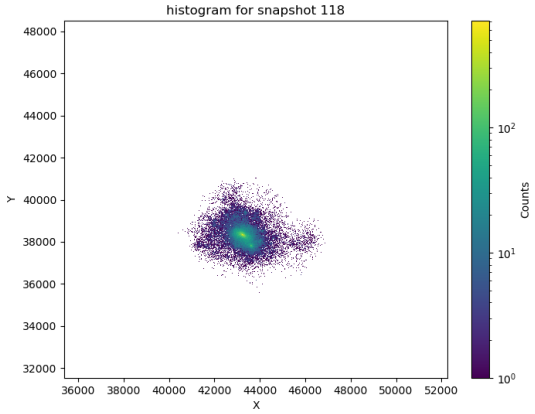


(f) Subhalo 1890: snapshot 118, at $z = 0.23$

Figure 29: Subhalo 1890 selected histograms

## A.4 Subhalo 574

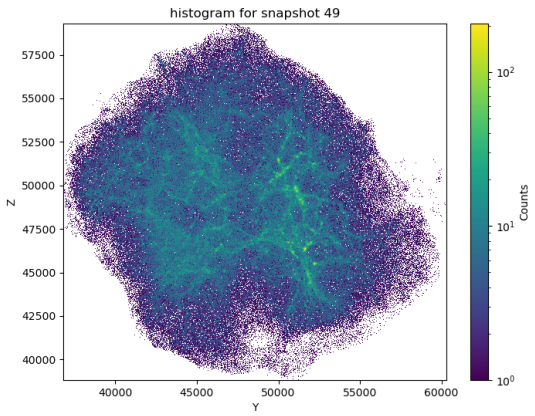


(a) Subhalo 574: snapshot 49 at $z = 5.00$

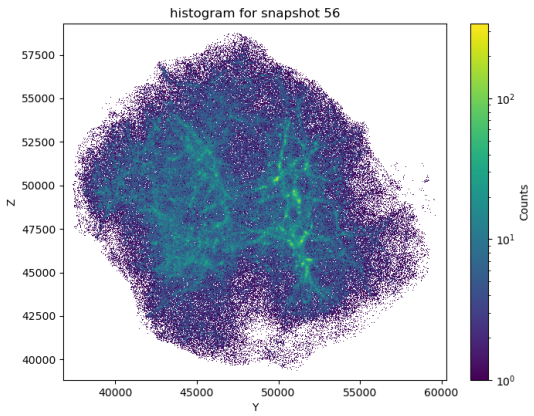


(b) Subhalo 574: snapshot 56, at $z = 3.71$

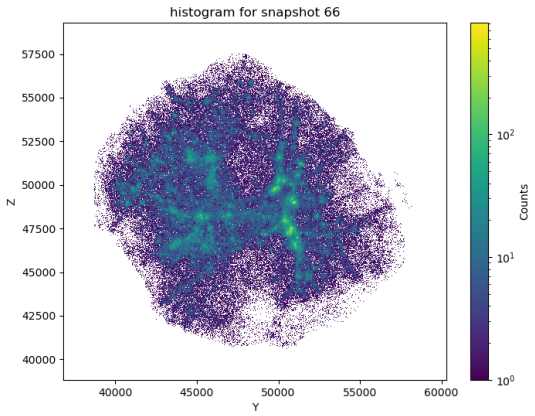


(c) Subhalo 574: snapshot 66, at $z = 2.21$

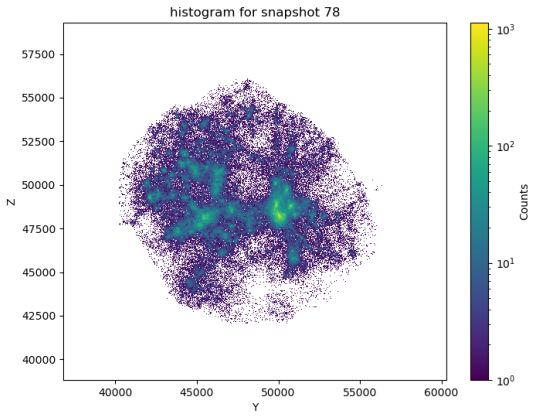


(d) Subhalo 574: snapshot 78, at $z = 1.30$

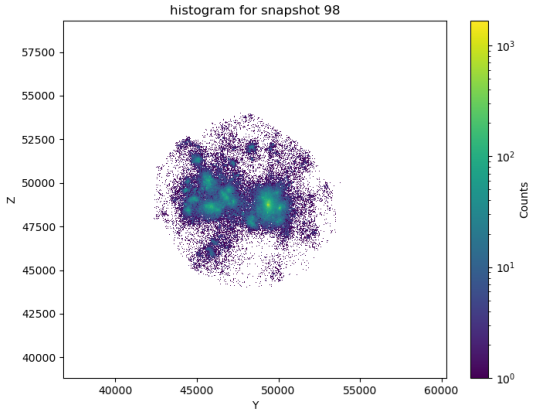


(e) Subhalo 574: snapshot 98, at $z = 0.62$

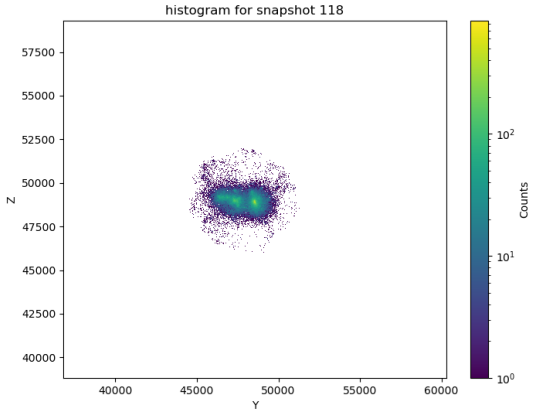


(f) Subhalo 574: snapshot 118, at $z = 0.23$

Figure 30: Subhalo 574 selected histograms

## B NEXUS+ Identifications

This section offers additional images of NEXUS+ MMF identifications.

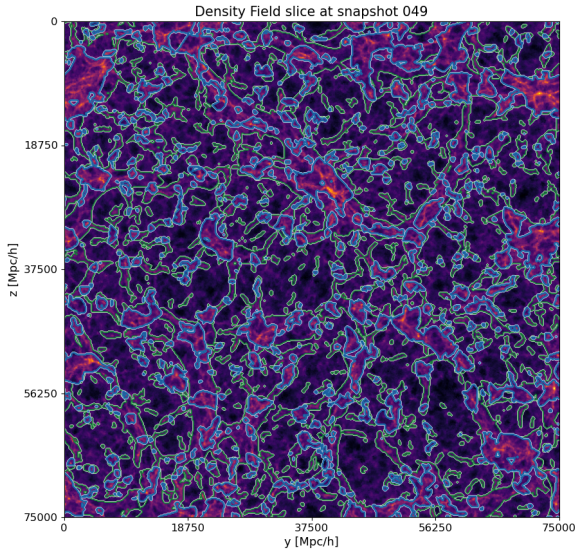


(a) Slice with NEXUS+ identifications at $z = 5.00$

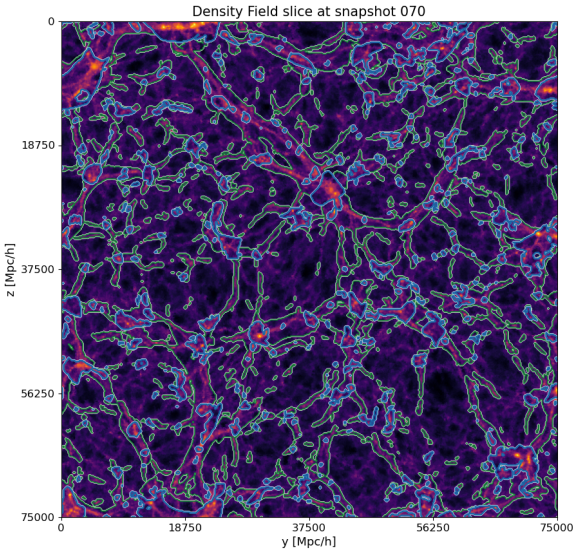


(b) Slice with NEXUS+ identifications at $z = 1.82$

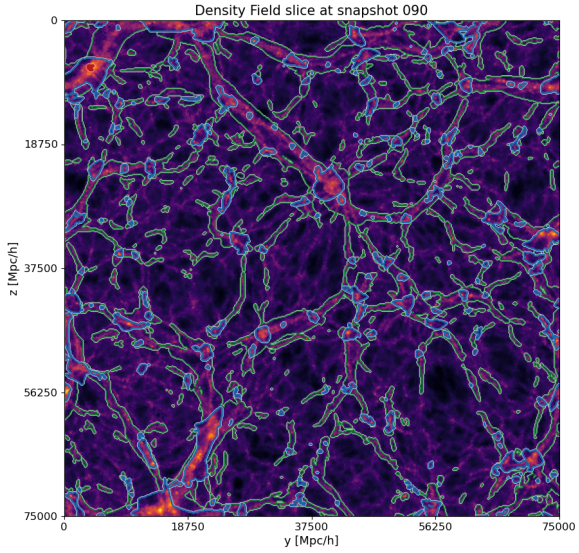


(c) Slice with NEXUS+ identifications at $z = 0.85$

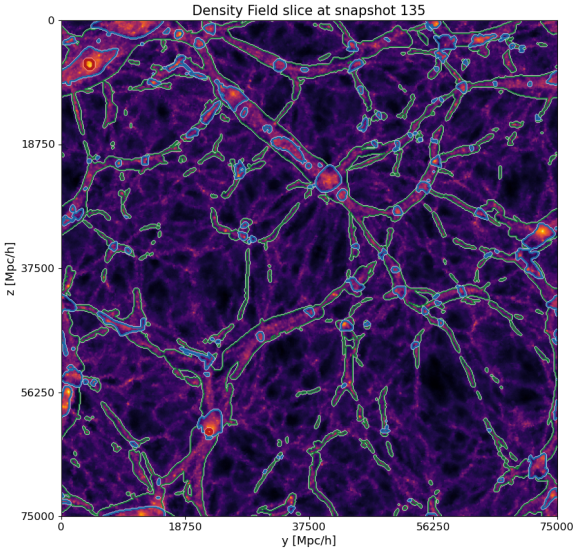


(d) Slice with NEXUS+ identifications at $z = 0.00$

# C Coding Appendix

## C.1 Mass Transport

To obtain the mass transport quantification, I concatenated the identified environments of all particles, per particle ID, in one big ‘pandas.DataFrame‘, as per figure 32

| | particle_type_135 | particle_type_133 | particle_type_131 | particle_type_129 | particle_type_127 | particle_type_125 | particle_type_123 |
|---|---|---|---|---|---|---|---|
| **3454907** | n | n | n | n | n | n | n |
| **88038007** | n | n | n | n | n | n | n |
| **3454932** | n | n | n | n | n | n | n |
| **88043982** | n | n | n | n | n | n | n |
| **2455757** | n | n | n | n | n | n | n |
| **...** | ... | ... | ... | ... | ... | ... | ... |
| **94196367** | v | v | v | v | v | v | v |
| **94196368** | v | v | v | v | v | v | v |
| **94196369** | f | f | f | f | f | f | f |
| **94196373** | w | w | w | w | w | w | w |
| **94196375** | w | w | w | w | w | w | w |

94196375 rows × 31 columns

Figure 32: Identified environments at all snapshots per particle ID dataframe

This was a dataset so big that there was not enough memory in the local computer cluster to allocate for concatenating. Two solutions to this were implemented: the index was stored as ‘uint-32‘ instead of ‘uint-64‘ as was the standard for ’pandas.DataFrame’; and the identifications were stored as categories, a ’pandas.DataFrame’ data type. This yielded a 16x decrease in working memory necessary. The catorisation of the identifiers also allowed me to use the ‘pandas.DataFrame.value_counts()‘ method. This was very convenient, as I could use it to find for instance, for particles of the type ’v’ at snapshot 135, what are the fractions of all other identifiers at different snapshots. This is exactly a quantification of how mass moves from one structure type to another:

1. we selected our environment type (‘env_base‘) at some snapshot ‘base_snapshot‘
2. we select the other snapshots (‘snapshot_list‘) that we are interested in
3. we obtain, per snapshot in ‘snapshot_list‘, what percentage of the particles that were in ‘env_base‘, were in all environments (see figure 33 for an example)
4. we can plot these percentages against the redhshift of the respective snapshot

Since we initially selected a particular environment, this filters out other particle IDs that were not in the respective environment at the selected redshift. From then on the ‘value_counts()‘ looks at the selected IDs, telling us how many of those initial particles were found in which type of environment at the other snapshots, completely synonymous to the common mass fraction described in equation 9.

| | n | f | w | v |
|---|---|---|---|---|
| **135** | 1.000000 | 0.000000 | 0.000000 | 0.000000 |
| **133** | 0.928267 | 0.071203 | 0.000516 | 0.000014 |
| **131** | 0.864710 | 0.134151 | 0.001100 | 0.000040 |
| **129** | 0.798929 | 0.198769 | 0.002181 | 0.000122 |
| **127** | 0.728233 | 0.267532 | 0.004138 | 0.000097 |
| **125** | 0.679569 | 0.313510 | 0.006729 | 0.000191 |
| **123** | 0.615977 | 0.373785 | 0.010012 | 0.000226 |
| **122** | 0.586412 | 0.401534 | 0.011844 | 0.000210 |

Figure 33: environment percentages, per snapshot, in relation to base snapshot 135